A Thermoelastic Analysis of Dislocation Generation in Pulled GaAs Crystals

By A. S. JORDAN, R. CARUSO, and A. R. VON NEIDA

(Manuscript received August 31, 1979)

The optical and electronic characteristics of devices based on GaAs (LEDs, laser diodes, etc.) are adversely affected by the dislocations originating in the substrates. We demonstrate by means of thermoelastic analysis that the primary cause for the observed dislocation density patterns in Czochralski-pulled GaAs single crystals, which serve as a source for substrates, is crystallographic glide, induced by the excessive thermal stresses arising during the growth process. First, we formulate a tractable model for crystal growth. We obtain the temperature distribution in the crystal by solving the quasi-steady-state partial differential equation for heat conduction subject to appropriate boundary conditions. The closed-form solution includes time, pull rate, axial location, radius, convective and radiative heat transfer coefficients ($h_r + h_c$), and a fixed ambient temperature (T_a) among the variables. Next, from the temperature profiles we determine the radial, tangential, and axial stress components acting on the GaAs boule. These stresses permit the evaluation of the 12 resolved shear stress components for the $\{111\}$, $\langle 1\bar{1}0 \rangle$ slip system. We postulate the sum of the absolute values of the 12 components (σ_{tot}) to be proportional to the dislocation density within an additive constant. Employing σ_{tot} as a parameter, we have constructed dislocation distribution contour maps for $\{100\}$ GaAs wafers which are in good accord with the dislocation patterns observed on KOH-etched wafers cut from near the top end of Cr and Te-doped GaAs boules. A detailed examination of the effect of the numerous parameters on the dislocation density of Czochralski-pulled GaAs is also given. Only by a drastic increase of T_a and a substantial decrease of $h_r + h_c$ would one be able to overcome the natural limitations imposed by the thermal and mechanical properties on dislocation density. Finally, we pay attention to the effects of elastic anisotropy and interfacial heat flux, discuss the philosophical and mathematical difficulties

associated with finding a true transient solution, and provide some practical suggestions.

I. INTRODUCTION

A number of recent papers have shown that the performance of GaAs-based devices is adversely affected by dislocations. For example, Brantley and Harrison[1] have observed that the degradation rate in diffused electroluminescent diodes increased by an order of magnitude, and was accompanied by dislocation generation, during forward bias aging when a compressive load was also applied. Subsequently, Zaeschner[2] has found that external stress alone is sufficient to cause diode degradation and gave a quantitative account of the change in light output with time in terms of the kinetic properties (multiplication and velocity) of dislocations, considered to be nonradiative recombination centers.

Even in the absence of deliberately imposed forces, a large enough density of grown-in dislocations in GaAs alters device behavior. In particular, very recently Roedel et al[3] have correlated the reduction in external quantum efficiency of Si-doped GaAlAs LEDs with increasing dislocation density and established that these defects act as nonradiative recombination centers. Moreover, the dislocation density in the GaAlAs epitaxial layer essentially duplicated that of the GaAs substrate. Therefore, in view of its importance, we have undertaken an investigation of the primary cause for the generation of dislocations in GaAs substrates grown by the Czochralski technique and then attempt to employ this knowledge in suggesting growth conditions which facilitate the elimination or at least reduction of these defects.

Some plausible mechanisms by means of which dislocations can be incorporated into growing GaAs boules are (*i*) dislocation propagation and multiplication from an imperfect seed, (*ii*) vacancy condensation into dislocation loops, and (*iii*) crystallographic glide relieving excessive thermal stresses. It has been recognized relatively early in the course of semiconductor crystal growth that thermal stresses may lead to slip and dislocation generation. In 1955, Billig[4] discovered that the etch pit density of Ge wafers, obtained from pulled ingots, increased with the magnitude of the imposed temperature gradient. Furthermore, the pits (representing the dislocations) were distributed in a definite pattern and slip bands were also observed. On the basis of these experiments, Billig concluded that high thermal stresses* gave rise to slipping and dislocation generation. He also made an order-of-magnitude estimate of the thermal stress to offer a more quantitative

---

* The stress was given by the product of the thermal expansion coefficient, Young's modulus, and the radial temperature drop.

underpinning to the postulated mechanism. The required temperature difference between the core and the edge of the crystal was obtained from a standard heat transfer calculation for a semi-infinite cylinder in the steady state. The base of the cylinder is at the melting point, T_f, while the sides are dissipating the heat by convection.

Almost simultaneously with Billig, Bennett and Sawyers[5] of Bell Laboratories found a hexagonal "star pattern" of pits along definite lines on etched Ge slices cut from $\langle 111 \rangle$ pulled ingots and gave the following qualitative description of the thermal stress effect: The heat enters the growing Ge crystal at the solid-liquid interface and leaves through the other surfaces by radiation and convection. Hence, each cross section of the crystal must have a cooler periphery than core and, consequently, on account of thermal contraction, the periphery must be in tension and the core in compression. If the resolved shear stress components of the $\{111\}$, $\langle 1\bar{1}0 \rangle$ slip system resulting from this tension are sufficiently high, then the resulting plastic deformation would exhibit the symmetry of the observed dislocation pattern.

In 1958, Penning[6] reported that etch pit arrays in germanium can also be introduced by radial heat flow during slow cooling from 850°C. The patterns show a crystallographic orientation-dependent symmetry and the dislocation density is highest at the edge, intermediate in the center, and lowest along an internal annulus. Following the earlier work, Penning also interpreted his results in terms of thermal stresses and formulated a semiquantitative model. In his view, it is reasonable to assume that two alternative avenues of stress relief are open to the crystal. In one case, the strain is entirely plastic and is completely relieved by the generation and motion of dislocations. In the other case, the thermal stress is mostly elastic, but a small constant fraction is released by plastic flow; hence, the dislocation density corresponding to one of the 12 $\{111\}$, $\langle 1\bar{1}0 \rangle$ slip systems is proportional to the amount of slip, governed by the appropriate shear strain component. A comparison of the observed and estimated etch patterns favors the path of incomplete stress relief.

Unfortunately, Penning[6] withheld the details of his assumptions and treatment for a promised forthcoming paper. To the best of our knowledge, that paper has not been published in the intervening 20 years. However, it seems clear from the brief account given in Ref. 6 that his calculations employed a simple parabolic temperature distribution in the crystal and the predicted etch figures were based on the shear components of the thermal stresses. In our view, even today, Penning's conceptual framework presents the most fruitful starting point in crystal-growth related thermal stress analysis.

A strong confirmation of plastic deformation taking place in semi-conductors during the growth cycle was provided by the work of

Lederhandler,[7] who correlated infrared birefringence with etch pit density in ⟨111⟩ Si. This investigation shows that the source of birefringence is the elastic-plastic deformation occurring under the influence of a radial temperature gradient. The frozen-in stress seen by birefringence is acquired by the crystal near room temperature and is equal and opposite to the thermal stress relieved by dislocations and plastic flow during growth. According to a more recent study, similar to germanium, the dislocation density in silicon exhibits a minimum at a location intermediate between the core and the lateral surface.[8]

Although the dislocation density in III-V compounds is occasionally orders of magnitude greater than in germanium and silicon, there is a paucity of information on the source of grown-in dislocations in the semiconducting compounds. In the case of liquid-encapsulation Czochralski-(LEC) grown GaP, Nygren[9] has found that, consistent with the thermal stress mechanism of dislocation generation, their density increases toward the periphery of the ingot; he also observed traces of slip. Moreover, the "frozen-in" stress was determined on the transparent crystal by a photoelastic technique showing equal tangential and radial stresses at the core and a disappearance of the radial stress at the periphery.

However, there is a lack of consensus with respect to the genesis of dislocations in GaAs. Based on their results using a modified Gremmelmaier-type magnetic puller, Steinemann and Zimmerli[10] claimed that thermal strain is inconsequential in causing dislocation generation. But they admitted that the omission of a heat shield from their apparatus made the growth of 1-cm diameter, low-dislocation density GaAs impossible even when a long neck was employed to eliminate the dislocations arising from the seed. Under these unfavorable conditions, the dislocation density increases toward the external surface.

Subsequently, Brice[11,12] has identified the partial pressure of arsenic (As$_4$) as an important contributing factor to the observed dislocation densities in GaAs. Crystals grown by the horizontal Bridgman method,[11] and in a syringe puller[12] at pressures between 0.8 and 1.3 atm, show a corresponding monotonic increase in their dislocation densities, probably as a result of gallium-vacancy condensation into dislocation loops.[11] Nonetheless, Brice has also suggested[12] that the radial temperature gradient via the thermal stress mechanism is responsible for the enhanced dislocation density near the edge of his crystals and surmised that, at lower pressures, the same mechanism may be responsible for the entire distribution. This latter notion is supported by Plaskett et al[13] who examined, by etching and x-ray topography, the slip line patterns of GaAs crystals grown by the horizontal Bridgman method at pressures somewhat below 1 atm. They concluded that the dislocations were created by plastic deformation arising from thermal stresses.

Therefore, in view of two decades of accumulated experience in the area of the melt growth of semiconducting crystals, it is reasonable to propose that the initial formation of dislocations in GaAs crystal pulled from stoichiometric melts by the Czochralski technique is primarily due to the excessive thermal stresses associated with the growth process. A major objective of this paper is to test this proposition by the formulation and analysis of a tractable model for growth which describes the dislocation distribution in terms of material and growth system parameters, thus permitting a direct comparison with experimentally derived dislocation patterns. As a first step, we require realistic temperature profiles for a growing ingot. A simple steady-state heat transfer model introduced by Brice[14] has given the experimental temperature distribution in germanium[14] and $ZnWO_4$,[15] obtained by a thermocouple embedding technique, in a consistent manner. He assumed that the growing crystal can be represented by a stationary cylinder, the base of which is held at T_f, while its lateral surface and top dissipate the heat into a medium at a constant temperature by convection and found the solution in the classic monograph of Carslaw and Jaeger.[16] However, this solution is only valid for a fixed ambient temperature and excludes growth rate as a parameter. In the present work, we have been able to include growth rate in the solution because a moving boundary quasi-steady-state, partial differential equation for heat conduction is considered instead of a steady-state one. In a future paper, we shall report the exact solution of the steady-state partial differential equation subject to convective heat transfer from the sides of the cylinder into an ambient with a linear temperature profile which abruptly changes slope at some height. Obviously, that result closely corresponds to the thermal geometry of LEC growth wherein a sharp break in temperature occurs at the B_2O_3-gaseous ambient interface.

The quasi-steady-state temperature profiles are used in deducing the radial, tangential, and axial thermal stress components for a growing cylinder in a closed form. Then these stresses are employed in evaluating the 12 resolved shear stress components of the $\{111\}$, $\langle 1\bar{1}0 \rangle$ slip system causing glide. Invoking Penning's hypothesis,[6] the dislocation density is taken to be proportional to the sum of these shear stresses. Computer simulation of the theoretical results is facilitated by some numerical techniques. Among these, we concentrate on the inversion of the formula for shear stress as a function of radius and angle into a polar plot of dislocation density contour lines.

Next, model calculations for the dislocation density patterns are presented, which show the effect of a realistic variation in the heat transfer coefficient, radius, pull rate, and time. Furthermore, the theoretical contours are compared to the dislocation density patterns exhibited by KOH-etched wafers. To ascertain that the GaAs crystal

encountered plastic flow above the critical resolved shear stress, consideration is given to the actual magnitude of the resolved shear stress in terms of the best estimates of the physical and geometrical parameters appropriate in the growth system. In addition, we discuss the possible effect of elastic anisotropy, the magnitude of the axial heat flux, and the philosophical difficulty of finding a true transient as opposed to a quasi-steady-state solution. Finally, some important conclusions are enumerated and practical suggestions are given to aid in the lowering of the dislocation density in GaAs.

II. THEORY

2.1 Quasi-steady-state partial differential equation for heat conduction during Czochralski growth

In general, severe mathematical problems are encountered in performing heat transfer calculations involving a change of state.[16,17] However, by an idealization of the Czochralski growth process, we can formulate a realistic but tractable model which permits the relatively uncomplicated determination of the time- and growth-rate-dependent temperature profiles prevailing during crystal growth. The following set of simplifying assumptions are introduced:

(*i*) Initially, at $t \leq 0$, the semi-infinite space between $z = 0$ and $-\infty$ is completely filled by a stoichiometric liquid solution of gallium and arsenic (melt) contained in a crucible and held at the melting point of GaAs, T_f (see Fig. 1).
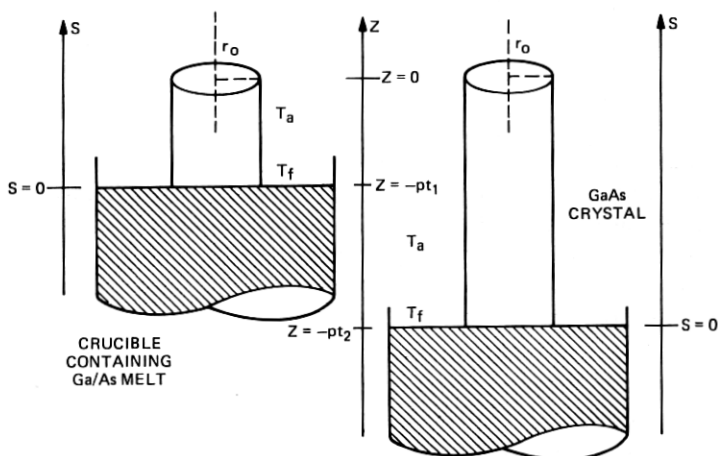

Fig. 1—Stationary (z) and moving (s) coordinate systems for Czochralski growth. The stationary and moving systems are anchored at the top (seed)-end and the solid-liquid interface, respectively. Above the interface, the temperature of the surroundings is uniformly T_a.

(*ii*) The crystal is grown by the removal of the crucible in the $-z$ direction at rate p, and its shape is cylindrical from top (seed) to bottom (tail).

(*iii*) The growing boule is surrounded by an ambient fluid at temperature T_a = constant $< T_f$, while the Ga/As melt is continuously maintained at T_f.

(*iv*) The planarity of the solid-liquid interface at T_f is essentially unchanged by the dissipation of the heat of fusion of GaAs.

(*v*) As the top of the crystal always remains stationary at $z = 0$ and the solid-liquid interface moves to $z = -pt$, the sense of growth is opposite that of the practical situation. This choice of direction is dictated by mathematical convenience, and it leaves the heat transfer unaffected as long as T_a is a constant.

(*vi*) The temperature distribution is not significantly influenced by crucible or crystal rotation.

(*vii*) At the top and on the lateral surface of the boule, the heat loss (flux) is proportional to the temperature difference between the surface and the ambient fluid. This is otherwise known as convection boundary condition governed by Newton's law of cooling.

Figure 1 sketches the coordinate system relevant to our Czochralski growth model. In the interest of clarity, the vertical axes (z and s) have been displaced from the crystal axes. In a cylindrical coordinate system (r, θ, z; t) with the origin at the center of the stationary crystal top, the partial differential equation for heat conduction takes the form

$$\frac{\partial T}{\partial t} = \kappa \left(\frac{\partial^2 T}{\partial r^2} + \frac{1}{r}\frac{\partial T}{\partial r} + \frac{\partial^2 T}{\partial z^2} \right), \qquad (1)$$

where κ(cm^2/s) is the thermal diffusivity. The diffusion equation is independent of θ on account of the cylindrical symmetry of the boundary conditions.

It is convenient to transform eq. (1) into a coordinate system (r, θ, s, τ) embedded in and moving with the solid-liquid interface to facilitate the application of the boundary condition $T = T_f$ at that location. This can be readily accomplished[18] by observing (Fig. 1) that

$$s = z + pt \qquad (2a)$$

$$\tau = t. \qquad (2b)$$

Noting that, from eqs. (2), $\partial s/\partial z = 1$, $\partial s/\partial t = p$, $\partial \tau/\partial z = 0$, and $\partial \tau/\partial t = 1$, the rules of partial differentiation yield[18]

$$\frac{\partial^2 T}{\partial z^2} = \frac{\partial^2 T}{\partial s^2} \quad \text{and} \quad \frac{\partial T}{\partial t} = p\frac{\partial T}{\partial s} + \frac{\partial T}{\partial \tau}. \qquad (3)$$

Substituting eqs. (3) into eq. (1), we have the partial differential

equation with respect to moving coordinate axes

$$\frac{\partial^2 T}{\partial r^2} + \frac{1}{r}\frac{\partial T}{\partial r} + \frac{\partial^2 T}{\partial s^2} = \frac{p}{\kappa}\frac{\partial T}{\partial s} + \frac{1}{\kappa}\frac{\partial T}{\partial \tau}. \tag{4}$$

According to Rosenthal's theory for moving heat sources,[19] an observer moving with the coordinate system fails to detect any change in temperature with time in his surroundings. Accordingly, $\partial T/\partial \tau = 0$ and eq. (4) reduces to

$$\frac{\partial^2 T}{\partial r^2} + \frac{1}{r}\frac{\partial T}{\partial r} + \frac{\partial^2 T}{\partial s^2} = \frac{p}{\kappa}\frac{\partial T}{\partial s}. \tag{5}$$

The preceding equation is called the partial differential equation for the quasi-steady state (QSS)[18, 19] and is expected to be valid after a crystal of some length has grown. The solution of the boundary value problem can be written in a simpler form by introducing the following dimensionless parameters:

$$\rho = \frac{r}{r_0}, \qquad \zeta = \frac{z}{r_0}, \qquad \psi = \frac{s}{r_0}. \tag{6}$$

Then eq. (5) becomes

$$\frac{\partial^2 T}{\partial \rho^2} + \frac{1}{\rho}\frac{\partial T}{\partial \rho} + \frac{\partial^2 T}{\partial \psi^2} = p_1\frac{\partial T}{\partial \psi}, \tag{7}$$

where

$$p_1 = pr_0/\kappa.$$

We attempt to separate the variables by substituting the product function

$$T = e^{p_1\psi/2}R(\rho)\Psi(\psi) \tag{8}$$

into eq. (7). The exponential factor in eq. (3) is based on Smoluchowski's solution for field-enhanced diffusion[20] wherein the differential equation is formally similar to eq. (7). Using eq. (8), eq. (7) separates into

$$\frac{d^2 R}{R d\rho^2} + \frac{1}{\rho R}\frac{dR}{d\rho} = \frac{p_1^2}{4} - \frac{1}{\Psi}\frac{d^2\Psi}{d\psi^2} = -\alpha^2, \tag{9}$$

where α is the separation constant.

It can be readily seen that the R differential equation, describing the radical variation in temperature, is given by

$$\frac{d^2 R}{d(\alpha\rho)^2} + \frac{dR}{\alpha\rho\, d\alpha\rho} + R = 0, \tag{10}$$

which is Bessel's differential equation of order zero.[21] Bessel functions of the first kind and order zero, $J_0(\alpha\rho)$ satisfy eq. (10) so that

$$R(\rho) = J_0(\alpha\rho). \tag{11}$$

The differential equation for the axial temperature distribution is

$$\beta^2 \Psi - \frac{d^2\Psi}{d\psi^2} = 0, \tag{12a}$$

where

$$\beta^2 = \alpha^2 + \frac{p_1^2}{4}. \tag{12b}$$

Obviously, the exponential function is a solution of eq. (12a). Hence, we can write, in general,

$$\Psi = A \sinh \beta(\psi_t - \psi) + B \cosh \beta(\psi_t - \psi), \tag{13a}$$

where

$$\psi_t = \frac{pt}{r_0} = \frac{\text{length}}{\text{radius}} \tag{13b}$$

and A and B are constants.

Since the value of the separation constant α is so far unrestricted, the complete solution of the QSS problem is obtained by means of eqs. (8), (11), and (13) in the form of the infinite sum

$$T = T_a + e^{p_1\psi/2} \sum_{n=1}^{\infty} J_0(\rho\alpha_n)[A_n\sinh \beta_n(\psi_t - \psi)$$

$$+ B_n\cosh \beta_n(\psi_t - \psi)]. \tag{14}$$

2.2 Boundary conditions

According to the previously outlined Czochralski growth model, at the top of the growing ingot and along the lateral surface, the heat is dissipated by Newtonian cooling. Expressed mathematically, this means that, at the cylindrical boundary,[16]

$$\frac{\partial T}{\partial r} + h(T - T_a)|_{r=r_0} = 0 \tag{15a}$$

or

$$\frac{\partial T}{\partial \rho} + h_1(T - T_a)|_{\rho=1} = 0, \tag{15b}$$

where $h = h_1/r_0$ is the heat transfer coefficient. On the stationary top

surface of the cylinder,

$$\frac{\partial T}{\partial s} + h(T - T_a)|_{s=p_t} = 0 \qquad (16a)$$

or

$$\frac{\partial T}{\partial \psi} + h_1(T - T_a)|_{\psi=\psi_t} = 0. \qquad (16b)$$

Applying eq. (15b) to eq. (14) leads to

$$\frac{dJ_0}{d\rho}(\alpha_n\rho) + h_1 J_0(\alpha_n\rho)|_{\rho=1} = 0. \qquad (17)$$

An important property of the Bessel functions of the first kind is the recursion formula[16,20]

$$\frac{dJ_0(x)}{dx} = -J_1(x), \qquad (18)$$

where J_1 is the Bessel function of order one. Rewriting eq. (17) in terms of eq. (18) provides the n characteristic equations

$$-\alpha_n J_1(\alpha_n) + h_1 J_0(\alpha_n) = 0 \qquad (19)$$

for the eigenvalues α_n. A combination of eqs. (16b) and (14) results in a relationship between A_n and B_n of the form

$$A_n = h_p \frac{B_n}{\beta_n}, \qquad (20a)$$

where

$$h_p = \frac{p_1}{2} + h_1. \qquad (20b)$$

Substituting eqs. (20a) into eq. (14), we obtain for the temperature profile of the growing ingot

$$T = T_a + e^{p_1\psi/2} \sum_{n=1}^{\infty} J_0(\alpha_n\rho) \frac{B_n}{\beta_n} [h_p \sinh \beta_n(\psi_t - \psi)$$

$$+ \beta_n \cosh \beta_n(\psi_t - \psi)], \quad (21)$$

where the $\alpha_n s$ are the eigenvalues of eq. (19).

We determine the remaining constant B_n from the boundary condition

$$T = T_f \qquad (22)$$

at the planar solid-liquid interface ($\psi = 0$). Then eq. (21) reduces to

$$T_f - T_a = \sum_{n=1}^{\infty} J_0(\alpha_n\rho) \frac{B_n}{\beta_n} [h_p \sinh \beta_n\psi_t + \beta_n \cosh \beta_n\psi_t]. \qquad (23)$$

To find B_n, we must expand the constant $T_f - T_a$ as a series in J_0. Based on the orthogonality properties of Bessel functions, subject to the characteristic eq. (19), it can be shown that an arbitrary function $f(\rho)$ can be expanded by means of the Bessel series[16]

$$f(\rho) = \sum_{n=1}^{\infty} K_n J_0(\alpha_n\rho), \qquad (24a)$$

where

$$K_n = \frac{2\alpha_n^2}{(h_1^2 + \alpha_n^2)J_0^2(\alpha_n)} \int_0^1 \rho f(\rho) J_0(\alpha_n\rho) \, d\rho. \qquad (24b)$$

Putting $f(\rho) = T_f - T_a$ and in view of another recursive property of Bessel functions,[16,20]

$$\frac{dx \, J_1(x)}{dx} = x J_0(x), \qquad (25)$$

eq. (24b) integrates to

$$K_n = \frac{2\alpha_n J_1(\alpha_n)(T_f - T_a)}{(h_1^2 + \alpha_n^2)J_0^2(\alpha_n)} = \frac{2h_1(T_f - T_a)}{(h_1^2 + \alpha_n^2)J_0(\alpha_n)}. \qquad (26)$$

Term-by-term evaluation of B_n is accomplished by a combination of eqs. (23), (24a), and (26). Then we find

$$B_n = \frac{2h_1(T_f - T_a)\beta_n}{(h_1^2 + \alpha_n^2)J_0(\alpha_n)} \times \frac{1}{h_p \sinh \beta_n\psi_t + \beta_n \cosh \beta_n\psi_t}. \qquad (27)$$

Finally, substituting eq. (27) into eq. (21), the QSS temperature distribution for Czochralski growth becomes

$$\frac{T - T_a}{T_f - T_a} = 2h_1 e^{p_1\psi/2} \sum_{n=1}^{\infty} \frac{J_0(\alpha_n\rho)}{(h_1^2 + \alpha_n^2)J_0(\alpha_n)}$$
$$\times \frac{h_p \sinh \beta_n(\psi_t - \psi) + \beta_n \cosh \beta_n(\psi_t - \psi)}{h_p \sinh \beta_n\psi_t + \beta_n \cosh \beta_n\psi_t} \qquad (28)$$

where the summation is over the n eigenvalues of eq. (19). It is convenient to repeat here the previously given definitions of the

variables and parameters occurring in eq. (28). These are

$$h_1 = hr_0, \; p_1 = \frac{pr_0}{\kappa}, \; h_p = \frac{p_1}{2} + h_1$$

$$\beta_n = \left(\alpha_n^2 + \frac{p_1^2}{4} \right)^{1/2}$$

$$\rho = \frac{r}{r_0}, \; \psi = \frac{z + pt}{r_0} \quad \text{and} \quad \psi_t = \frac{pt}{r_0}. \tag{29}$$

2.3 Thermal stress

The temperature distribution induces a thermal stress field in the growing cylindrical ingot as a result of spatially inhomogeneous thermal contraction. The appropriate stress components can be obtained from classical thermoelastic theory.[22] In essence, in this theory an additivity hypothesis of elastic and thermal strains is superimposed on Hooke's Law. There are only few exact solutions of the thermoelastic equations. However, for a long isotropic cylinder with axisymmetrical temperature distribution, an exact description of the stress components is possible if the displacement is only radial, the center suffers no displacement, and the lateral surface is free of traction.[22] This set of assumptions provides the so-called "plane strain" solution which is subsequently adjusted by means of Saint-Venant's principle to take into account the absence of traction at the top and bottom ends. Consequently, the following final expressions have been derived for the radial, σ_r, tangential, σ_θ, stress components:

$$\sigma_r = \frac{aE}{1 - \nu} \left(\frac{1}{r_0^2} \int_0^{r_0} Tr \, dr - \frac{1}{r^2} \int_0^r Tr \, dr \right) \tag{30a}$$

$$\sigma_\theta = \frac{aE}{1 - \nu} \left(\frac{1}{r_0^2} \int_0^{r_0} Tr \, dr + \frac{1}{r^2} \int_0^r Tr \, dr - T \right) \tag{30b}$$

$$\sigma_z = \frac{aE}{1 - \nu} \left(\frac{2}{r_0^2} \int_0^{r_0} Tr \, dr - T \right), \tag{30c}$$

where E, ν, and a are Young's modulus, Poisson's ratio, and the linear thermal expansion coefficient, respectively.[22]

To calculate the components explicitly, it is convenient to rewrite eqs. (30) in terms of the dimensionless variable ρ and integrate with respect to $\alpha_n \rho$. Then we have

$$\sigma_r = \frac{aE}{1-\nu}\frac{1}{\alpha_n^2}\left[\int_0^{\alpha_n} T\alpha_n\rho d(\alpha_n\rho) - \frac{1}{\rho^2}\int_0^{\alpha_n\rho} T\alpha_n\rho d(\alpha_n\rho)\right] \tag{31a}$$

$$\sigma_\theta = \frac{aE}{1-\nu}\frac{1}{\alpha_n^2}\left[\int_0^{\alpha_n} T\alpha_n\rho d(\alpha_n\rho) + \frac{1}{\rho^2}\int_0^{\alpha_n\rho} T\alpha_n\rho d(\alpha_n\rho) - \alpha_n^2 T\right] \tag{31b}$$

$$\sigma_z = \frac{aE}{1-\nu}\frac{1}{\alpha_n^2}\left[2\int_0^{\alpha_n} T\alpha_n\rho d(\alpha_n\rho) - \alpha_n^2 T\right]. \tag{31c}$$

All the integrals in eqs. (31) can be readily performed by applying eq. (25) to eq. (28). Hence, the stress components become

$$\sigma_r = 2h_1 e^{p_1\psi/2}\frac{aE}{1-\nu}(T_f - T_a)$$
$$\times \sum_{n=1}^{\infty}\frac{h_p\sinh\beta_n(\psi_t - \psi) + \beta_n\cosh\beta_n(\psi_t - \psi)}{(h_1^2 + \alpha_n^2)J_0(\alpha_n)(h_p\sinh\beta_n\psi_t + \beta_n\cosh\beta_n\psi_t)}$$
$$\times \left[\frac{J_1(\alpha_n)}{\alpha_n} - \frac{J_1(\alpha_n\rho)}{\alpha_n\rho}\right] \tag{32a}$$

$$\sigma_\theta = 2h_1 e^{p_1\psi/2}\frac{aE}{1-\nu}(T_f - T_a)$$
$$\times \sum_{n=1}^{\infty}\frac{h_p\sinh\beta_n(\psi_t - \psi) + \beta_n\cosh\beta_n(\psi_t - \psi)}{(h_1^2 + \alpha_n^2)J_0(\alpha_n)(h_p\sinh\beta_n\psi_t + \beta_n\cosh\beta_n\psi_t)}$$
$$\times \left[\frac{J_1(\alpha_n)}{\alpha_n} + \frac{J_1(\alpha_n\rho)}{\alpha_n\rho} - J_0(\alpha_n\rho)\right] \tag{32b}$$

$$\sigma_z = 2h_1 e^{p_1\psi/2}\frac{aE}{1-\nu}(T_f - T_a)$$
$$\times \sum_{n=1}^{\infty}\frac{h_p\sinh\beta_n(\psi_t - \psi) + \beta_n\cosh\beta_n(\psi_t - \psi)}{(h_1^2 + \alpha_n^2)J_0(\alpha_n)(h_p\sinh\beta_n\psi_t + \beta_n\cosh\beta_n\psi_t)}$$
$$\times \left[\frac{2J_1(\alpha_n)}{\alpha_n} - J_0(\alpha_n\rho)\right]. \tag{32c}$$

It should be noted that eqs. (31) are not changed by an additive constant (T_a).

2.4 Resolved shear stress

The major mechanism by means of which dislocations are first introduced during the Czochralski growth of GaAs is crystallographic glide caused by the excessive thermal stress. According to Schmid's Law,[23] glide occurs when the resolved shear stress (σ_{RS}) exceeds a certain critical value, the so-called critical resolved shear stress. Since the dislocation density, $d_\perp$, is proportional to the glide strain, we may also take it to be proportional to the σ_{RS} within an additive constant.

It has been previously shown that slip in GaAs is associated with the $\{111\}$, $\langle 1\bar{1}0\rangle$ slip system.[24] This is also the case for other semiconductors crystallizing in the diamond or zinc blende structure.[25] The $\{111\}$, $\langle 1\bar{1}0\rangle$ slip system represents 12 permissible glide operations, that is, four $\{111\}$ slip planes, each containing three possible $\langle 1\bar{1}0\rangle$ slip directions. In this section, we give σ_{RS} for each of the 12 distinct slip systems, obtained from the principal thermal stresses σ_r, σ_θ, and σ_z. The calculation is shown in detail for one system; the remaining 11 can be derived by analogous procedures and only the final results will be quoted.

The coordinate system appropriate to perform the stress transformations is presented in Fig. 2. To begin, it is necessary to determine the stress components acting on the xy, xz, and yz coordinate planes.
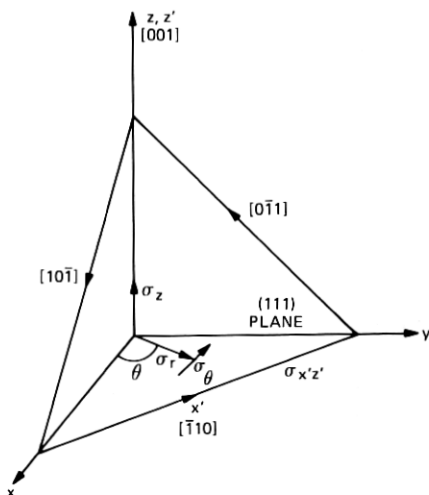

Fig. 2—Coordinate system for thermal stress transformations. For a crystal growing in the [001] orientation, the direction of the radial (σ_r), tangential (σ_θ), and axial (σ_z) components of the thermal stresses are shown. One of the 12 resolved shear stresses ($\sigma_{x'z'}$) is illustrated, which acts on the (111) slip plane in the [$\bar{1}$10] slip direction.

By standard tensor transformation,[26] we find

$$\sigma_x = \sigma_r \cos^2\theta + \sigma_\theta \sin^2\theta \tag{33a}$$

$$\sigma_y = \sigma_r \sin^2\theta + \sigma_\theta \cos^2\theta \tag{33b}$$

$$\sigma_{xy} = (\sigma_r - \sigma_\theta)\sin\theta\cos\theta \tag{33c}$$

$$\sigma_z = \sigma_z. \tag{33d}$$

As an illustrative example of the procedure followed, we calculate the σ_{RS} acting on the (111) plane in the $[\bar{1}10]$ slip direction. The coordinate system of the σ_{RS} is the x', y', z' system wherein z' and x' are parallel with the [111] normal and $[\bar{1}10]$, respectively. Then σ_{RS} becomes

$$\sigma_{RS} = \sigma_{x'z'} = \sigma_x \cos[x'x]\cos[z'x] + \sigma_y \cos[x'y]\cos[z'y]$$
$$+ \sigma_z \cos[x'z]\cos[z'z] + \sigma_{xy}(\cos[x'x]\cos[z'y]$$
$$+ \cos[x'y]\cos[z'x]), \tag{34}$$

where the extended notation has been used and the bracket signifies the angle between the indicated axes. In the [001] crystal growth direction, it is easy to evaluate the direction cosines; they are summarized as follows:

cos[ ]	x	y	z
x'	$-\sqrt{2}/2$	$\sqrt{2}/2$	0
y'			
z'	$\sqrt{3}/3$	$\sqrt{3}/3$	$\sqrt{3}/3$

A combination of eqs. (33), (34) and the table provides

$$(111), [\bar{1}10] \quad \sigma_{RS} = -\frac{\sqrt{6}}{6}(\sigma_r - \sigma_\theta)(\cos^2\theta - \sin^2\theta). \tag{35}$$

In a like manner, all the σ_{RS} can be evaluated. Introducing the abbreviation

$$\bar{\sigma}_r = \sigma_r - \sigma_\theta \tag{36a}$$

and

$$\bar{\sigma}_z = \sigma_z - \sigma_\theta \tag{36b}$$

and taking advantage of some standard trigonometric identities, the

following complete set of σ_{RS} is obtained:

Slip Plane	Slip Direction	σ_{RS}
(111)	[$\bar{1}$10]	$-\dfrac{\sqrt{6}}{6}\,\bar{\sigma}_r\cos 2\theta$
(111)	[0$\bar{1}$1]	$\dfrac{\sqrt{6}}{6}\left[\bar{\sigma}_z -\bar{\sigma}_r\sin^2\theta -\dfrac{\bar{\sigma}_r}{2}\sin 2\theta\right]$
(111)	[10$\bar{1}$]	$-\dfrac{\sqrt{6}}{6}\left[\bar{\sigma}_z -\bar{\sigma}_r\cos^2\theta -\dfrac{\bar{\sigma}_r}{2}\sin 2\theta\right]$
($\bar{1}$11)	[$\bar{1}$0$\bar{1}$]	$\dfrac{\sqrt{6}}{6}\left[\bar{\sigma}_r\cos^2\theta -\bar{\sigma}_z -\dfrac{\bar{\sigma}_r}{2}\sin 2\theta\right]$
($\bar{1}$11)	[0$\bar{1}$1]	$\dfrac{\sqrt{6}}{6}\left[\bar{\sigma}_z -\bar{\sigma}_r\sin^2\theta +\dfrac{\bar{\sigma}_r}{2}\sin 2\theta\right]$
($\bar{1}$11)	[110]	$-\dfrac{\sqrt{6}}{6}\,\bar{\sigma}_r\cos 2\theta$
($\bar{1}\bar{1}$1)	[011]	$\dfrac{\sqrt{6}}{6}\left[\bar{\sigma}_z -\bar{\sigma}_r\sin^2\theta -\dfrac{\bar{\sigma}_r}{2}\sin 2\theta\right]$
($\bar{1}\bar{1}$1)	[$\bar{1}$0$\bar{1}$]	$\dfrac{\sqrt{6}}{6}\left[\bar{\sigma}_r\cos^2\theta -\bar{\sigma}_z +\dfrac{\bar{\sigma}_r}{2}\sin 2\theta\right]$
($\bar{1}\bar{1}$1)	[1$\bar{1}$0]	$-\dfrac{\sqrt{6}}{6}\,\bar{\sigma}_r\cos 2\theta$
(1$\bar{1}$1)	[011]	$\dfrac{\sqrt{6}}{6}\left[\bar{\sigma}_z -\bar{\sigma}_r\sin^2\theta +\dfrac{\bar{\sigma}_r}{2}\sin 2\theta\right]$
(1$\bar{1}$1)	[10$\bar{1}$]	$\dfrac{\sqrt{6}}{6}\left[\bar{\sigma}_r\cos^2\theta -\bar{\sigma}_z -\dfrac{\bar{\sigma}_r}{2}\sin 2\theta\right]$
(1$\bar{1}$1)	[$\bar{1}\bar{1}$0]	$-\dfrac{\sqrt{6}}{6}\,\bar{\sigma}_r\cos 2\theta.$

$$\text{(37)}$$

Inspection of eqs. (37) shows that only five of the 12 stress equations are independent. Therefore, we define five σ_{RS} functions differentiated

by Roman numeral subscripts I through V and transform eqs. (37) into

Slip Plane	Slip Direction	σ_{RS}
(111)	$[\bar{1}10]$	
$(\bar{1}11)$	$[110]$	
$(\bar{1}\bar{1}1)$	$[1\bar{1}0]$	$\sigma_{\rm I} = -\dfrac{\sqrt{6}}{6}\,\bar{\sigma}_r \cos 2\theta$
$(1\bar{1}1)$	$[\bar{1}\bar{1}0]$	
(111)	$[0\bar{1}1]$	
$(\bar{1}\bar{1}1)$	$[011]$	$\sigma_{\rm II} = \dfrac{\sqrt{6}}{6}\left[\bar{\sigma}_z - \bar{\sigma}_r\dfrac{2}{\sqrt{2}}\sin\theta\sin(\theta + \pi/4)\right]$
$(\bar{1}11)$	$[0\bar{1}1]$	
$(1\bar{1}1)$	$[011]$	$\sigma_{\rm III} = \dfrac{\sqrt{6}}{6}\left[\bar{\sigma}_z - \bar{\sigma}_r\dfrac{2}{\sqrt{2}}\sin\theta\sin(\theta - \pi/4)\right]$
(111)	$[10\bar{1}]$	
$(\bar{1}\bar{1}1)$	$[\bar{1}0\bar{1}]$	$\sigma_{\rm IV} = -\dfrac{\sqrt{6}}{6}\left[\bar{\sigma}_z - \bar{\sigma}_r\dfrac{2}{\sqrt{2}}\cos\theta\sin(\theta + \pi/4)\right]$
$(\bar{1}11)$	$[\bar{1}0\bar{1}]$	
$(1\bar{1}1)$	$[10\bar{1}]$	$\sigma_{\rm V} = -\dfrac{\sqrt{6}}{6}\left[\bar{\sigma}_z + \bar{\sigma}_r\dfrac{2}{\sqrt{2}}\cos\theta\sin(\theta - \pi/4)\right]$

$$\tag{38}$$

where we have also employed trigonometric angle-sum relations.

Finally, since slip occurs regardless of the sign of σ_{RS}, we take the dislocation density to be proportional within an additive constant to the quantity $\sigma_{\rm tot}$ which is defined as the sum of the absolute values of the $12\sigma_{RS}$'s acting in the $\{111\}$, $\langle 1\bar{1}0\rangle$ slip system. Such correlation clearly implies that the stresses are mostly elastic which are not completely relieved by plastic flow.[6] Therefore, we have the proportionality

$$d_\perp \propto \sigma_{\rm tot} \equiv 4\,|\sigma_{\rm I}| + 2[\,|\sigma_{\rm II}| + |\sigma_{\rm III}| + |\sigma_{\rm IV}| + |\sigma_{\rm V}|\,]. \tag{39}$$

Of course, $\sigma_{\rm tot}$ can be explicitly obtained by sequential substitutions from eqs. (38), (36), and (32) into eq. (39).

III. COMPUTING METHODS

To investigate the effect of material and growth system parameters on the dislocation distribution in GaAs ingots grown by the Czochralski technique, the closed form solutions for the temperature profile [eq. (28)], thermal stress components [eqs. (32)], and the sum of the resolved shear stresses [eq. (39)] must be evaluated and displayed in suitable graphical forms. An essential function in these equations is the Bessel function of the first kind orders zero (J_0) and one (J_1). In principle, they can be obtained from Taylor series representations;[21] however, for large arguments the convergence of the series is very

slow. Fortunately, Abramowitz and Stegun[27] provide useful algorithms for both J_0 (their eqs. 9.4.1 and 9.4.3) and J_1 (their eqs. 9.4.4 and 9.4.6) with an accuracy of better than 10^{-7}.

Summation of the Bessel functions over the complete spectra of the eigenvalues α_n is required by all our results of interest. The characteristic equation [eq. (19)] immediately suggests not only that α_n is a function of h_1 but also that if $h_1 \to 0$, α_n is the root of $J_1(\alpha_n) = 0$, while as $h_1 \to \infty$, α_n is the root of $J_0(\alpha_n) = 0$. Therefore, the characteristic equation has as many roots as the Bessel functions themselves, i.e., their number increases to infinity. Since the first root α_1 at $h_1 \to 0$ occurs at $J_1(\alpha_1) = 0$, $\alpha_1 \to 0$, it is necessary to derive the limiting expression for α_1 for small h_1 from a Taylor series expansion of eq. (19). Then we find

$$\alpha_1 = 2\sqrt{\frac{2h_1}{4 + h_1}}, \tag{40}$$

which is very accurate up to $h_1 \simeq 0.1$. For larger values of h_1 and α_i up to $i = 6$, a numerical table for the roots of the characteristic equation is given by Carslaw and Jaeger.[16] These results can be adapted for computer use by parabolic least-square fits in h_1* which we find to be accurate within better than 100 parts per million up to $h_1 < 3$.

In view of the inverse α_n^2 dependence observed in our key expressions, typically six terms were judged to be adequate to obtain convergent sums in α_n. If, however, functional values very near the solid-liquid interface are of interest, a certain caution is warranted. It can be readily shown with reference to eq. (28) that, if ψ_t is large (long boule), the radial part of the function is multiplied by the approximate quantity $e^{-\beta_n \psi}$. At the top of the crystal ψ is sizable; hence, as β_n increases with n, $e^{-\beta_n \psi}$ readily tends to zero. In contrast, if ψ is small (near the solid-liquid interface), many additional $e^{-\beta_n \psi}$ terms are needed to achieve convergence.

The preceding considerations permit the evaluation of the temperature profiles in the growing ingot according to eq. (28). Since T_f is a constant value while T_a is an adjustable parameter, it is more convenient to present the complement of $T - T_a/T_f - T_a$, i.e.,

$$1 - \frac{T - T_a}{T_f - T_a} = \frac{T_f - T}{T_f - T_a} \tag{41}$$

so that the temperature is always referred to a true constant. In Fig. 3, $T_f - T/T_f - T_a$ is shown as a function of the dimensionless radius $\rho = r/r_0$ and distance $-z/r_0 = \psi_t - \psi$ from the top of the crystal at $h = 0.3$ and 0.6 cm^{-1}. It is advantageous to employ $-z/r_0$ for the axial

---

* A sixth power for α_1 and a second power fit for α_2 through α_6 were used.
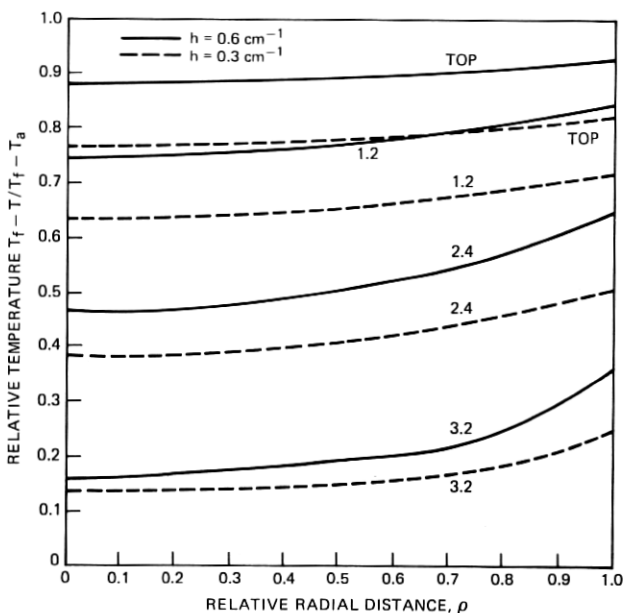
Fig. 3—Relative temperature drop $(T_f - T/T_f - T_a)$ versus relative radial distance $(\rho = r/r_0)$ for GaAs at $h = 0.3$ and 0.6 cm^{-1} [eq. (28)]. The labels are the distances in centimeters from the top of the crystal. Other relevant parameters are $t = 3600$ s, $p = 0.001$ cm/s, length $= 3.6$ cm, $r_0 = 2$ cm, and $\kappa = 0.04$ cm^2/s. Multiplication by $T_f - T_a$ provides the temperature decrease with respect to the melting point (1238°C) of GaAs.

coordinate since it designates at all times an invariant location in the ingot. It can be seen in Fig. 3 that increasing h leads to enhanced cooling at the same position and also to a sharper radial temperature gradient toward the periphery of the crystal.

The radial, tangential, and axial thermal stresses, obtained from eqs. (32), normalized to $(aE/1 - \nu)[(T_f - T_a)/200]$ are presented in Fig. 4, as functions of ρ and $-z/r_0$ at $h = 0.6$. In accord with the qualitative observations in Section I, the stress components are compressive at the core, while the outer surface is in tension ($\sigma_\theta = \sigma_z > 0$, $\sigma_r = 0$). The stress components in Fig. 4 give rise to σ_{tot} the sum of the absolute values of σ_{RS} acting in the $\{111\}$, $\langle 1\bar{1}0 \rangle$ slip system, which is taken to be proportional to the dislocation density of a $\langle 100 \rangle$ crystal. In Fig. 5, we show the radial and axial variation of σ_{tot} normalized to $(aE/1 - \nu)[(T_f - T_a)/200]$ at $h = 0.6$ in the $\langle 100 \rangle$ as well as $\langle 110 \rangle$ directions. It should be noted that in consonance with experimental results for Si[8] and Ge,[6] there is a density minimum at $\rho \simeq 0.6$ and the core is more perfect than the periphery. Moreover, apart from the core, the dislocation density is always higher along the $\langle 100 \rangle$ than the $\langle 110 \rangle$ direction.

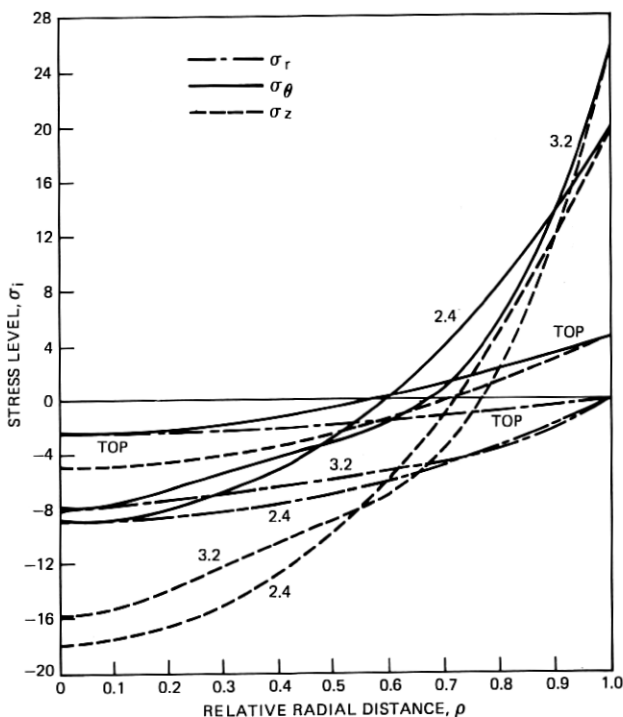Although Fig. 5 provides an acceptable graphical representation of

DISLOCATION GENERATION IN GaAs CRYSTALS **611**

Fig. 4—Radial (σ_r), tangential (σ_θ), and axial (σ_z) stress levels versus relative radial distance ($\rho = r/r_0$) for GaAs at $h = 0.6$ cm^{-1} [eqs. (32)]. Multiplication of the levels by $(\alpha E/1 - \nu)[(T_f - T_a)/200]$ yields the stresses in absolute units. The labels are the distances in centimeters from the top of the crystal. Other relevant parameters are $t = 3600$ s, $p = 0.001$ cm/s, length $= 3.6$ cm, $r_0 = 2$ cm, and $\kappa = 0.04$ cm^2/s.

the thermal stress effect on dislocation distribution in some directions, it does not allow a ready visualization of the distribution over an entire wafer surface. Obviously, an explicit plot based on eq. (39) can either illustrate σ_{tot} as a function of ρ at a constant angle θ (as in Fig. 5) or as a function of θ at a series of fixed ρs.* What one thus needs to serve as a ready standard of comparison with experimental information on etched wafers is a polar plot of ρ versus θ at constant levels of σ_{tot}. Since an exact inversion of eq. (39) in this manner is impossible, a numerical formulation to give ρ as a function of σ_{tot} at a constant θ must be attempted. The inversion method adopted takes into account the fact that any curve in Fig. 5 possesses a slowly descending lower branch up to $\rho \simeq 0.6$ and a more rapidly increasing upper branch to $\rho = 1$. Along the upper branch $\rho = f(\sigma_{tot}; \psi, \theta, h, p, t = $ constant) can be represented by a parabolic least-square fit of degree four. The excel-

---

* $\theta = 0$ and 45 degrees correspond to the ⟨100⟩ and ⟨110⟩ directions, respectively.
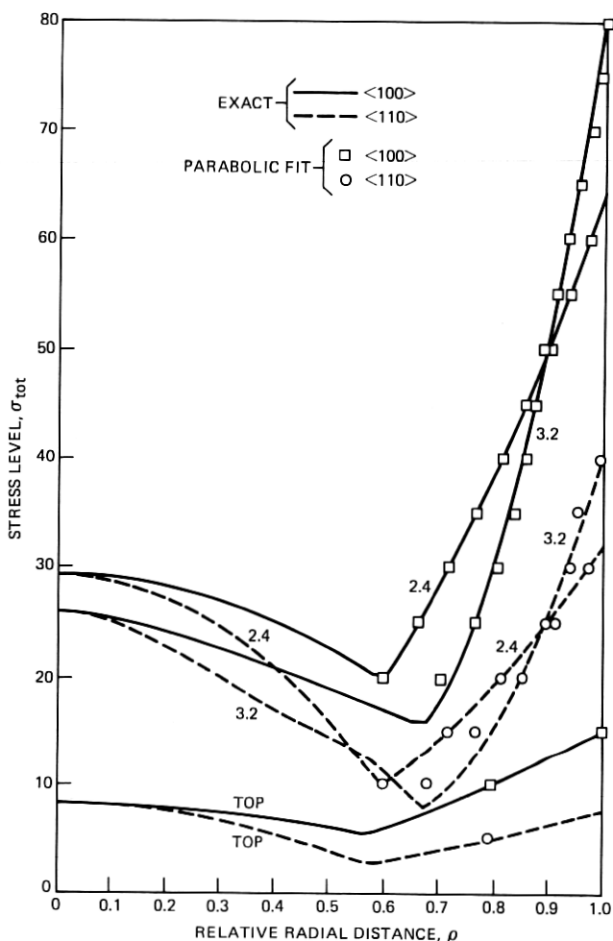
Fig. 5—Sum of the absolute values of the 12 resolved shear stress levels (σ_{tot}) or dislocation density versus relative radial distance ($\rho = r/r_0$). The variation in σ_{tot} is shown in the $\langle 100 \rangle$ and $\langle 110 \rangle$ directions of an $\langle 001 \rangle$ wafer. Multiplication of the levels by $(aE/1 - \nu)[(T_f - T_a)/200]$ yields the stress in absolute units. Relevant parameters are $h = 0.6$ cm^{-1}, $t = 3600$ s, $p = 0.001$ cm/s, length = 3.6 cm, $r_0 = 2$ cm, and $\kappa = 0.04$ cm^2/s.

lence of the fit is shown by the superimposed dots along the explicitly evaluated curves in Fig. 5. The same type of numerical procedure is unsatisfactory along the lower branch due to the very slow change in σ_{tot} with ρ up to $\rho \simeq 0.2$. Therefore, in the lower segment, the ρ value corresponding to a set σ_{tot} was obtained by linear interpolation within ρ intervals of 0.025.

In practice, ρ versus σ_{tot} was evaluated at up to 20 equally spaced stress levels in 2.5-degree intervals. By interconnecting the points corresponding to the same constant σ_{tot}, a polar plot (ρ versus θ) of the

stress or dislocation density contours was constructed. Without dwelling in detail on the cumbersome logical choices demanded by the development of the plotting routine, at the very least, it should be pointed out that when occasionally near the minimum ($\rho \simeq 0.6$), at a given σ_{tot}, the parabolic fit to the upper branch yielded a ρ value smaller than the extrapolated one from the lower branch, the point corresponding to the lower branch was utilized.

In Fig. 6, we present the polar plot of the dislocation distribution for the top wafer of a $\langle 100 \rangle$ GaAs crystal pulled by the Czochralski technique. The growth conditions and the temperature and stress profiles are identical with those for $-z/r_0 = 0$ and $h = 0.6$ in Figs. 3, 4, and 5. The contour lines shown are equally spaced and normalized to $(\alpha E/1 - \nu)[(T_f - T_a)/200]$. As an artifact of the stress profile computation in $\theta = 2.5$-degree intervals, the upper and lower branches of the closed contours near the center of a quadrant do not intersect in a point as they theoretically should, but are interconnected by brief straight-line segments.

It can be seen that the dislocation distribution exhibits fourfold symmetry and that the $\langle 110 \rangle$ ($\theta = 45$ degrees) is a mirror direction. In
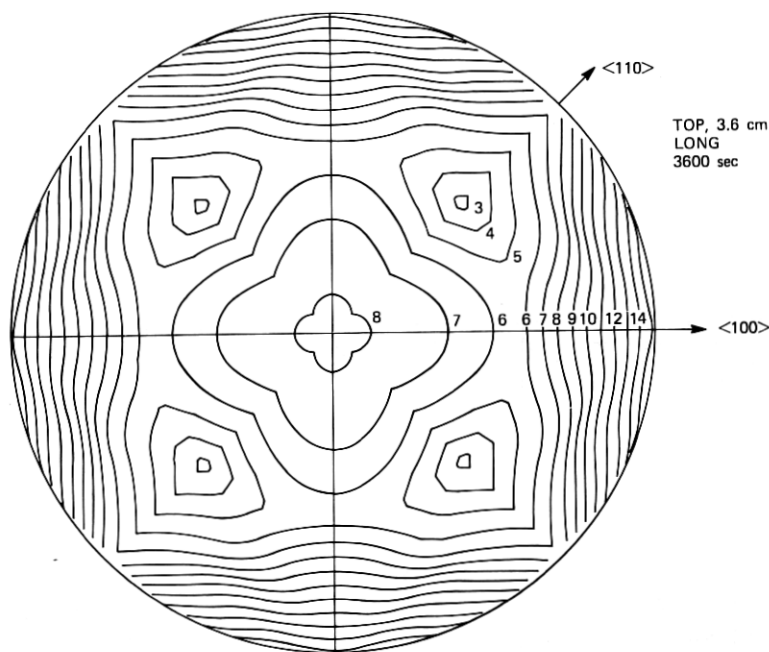
Fig. 6—Constant σ_{tot} or dislocation density contour lines for the top wafer of a $\langle 001 \rangle$ GaAs boule at $h = 0.6$ cm^{-1}. The σ_{tot} levels are labeled, which can be converted into absolute stresses when multiplied by $(aE/1 - \nu)[(T_f - T_a)/200]$. The appropriate parameters are $t = 3600$ s, $p = 0.001$ cm/s, length = 3.6 cm, $r_0 = 2$ cm, and $\kappa = 0.04$ cm^2/s.

all directions, there is a density minimum at $\rho \simeq 0.6$. Moreover, an absolute minimum in the pattern prevails along $\langle 110 \rangle$. In moving from the $\langle 110 \rangle$ to the $\langle 100 \rangle$ direction ($\theta = 0$), an increase in the density is observed. The crowding of the contours near the periphery of the crystal implies a sharp gradient in dislocation density, in accord with the previous experimental work summarized in the Introduction.

IV. RESULTS AND DISCUSSION

4.1 Estimation of the input parameters

Inspecting eqs. (28), (29), and (32), one can immediately realize that σ_{tot} and the resulting dislocation density pattern are affected by a number of parameters and independent variables. Consequently, it is necessary to obtain reasonable estimates for the values of these input parameters, in advance of a detailed examination with respect to their effect on σ_{tot}. In Table I, the range and/or value of these sundry quantities of interest are summarized, except for the heat transfer coefficient. Fortunately, the thermal and elastic properties are relatively insensitive to temperature change in the range near T_f. The data sources for Table I and the methods of evaluation and extrapolation will be given elsewhere.[28]

Perhaps the most important parameter is h, which is the constant of proportionality for Newtonian cooling on the cylindrical boundary and at the top of the crystal [eqs. (15a) and (16a)]. Since the crystal may lose heat by natural convection and/or thermal radiation, one has to resort to theoretical relations in fluid dynamics[29] and radiative transfer,[18] respectively, for guidance in the selection of h. For the purposes of this paper, the coefficient for heat transfer by a gas from a vertical

Table I—A summary of input parameters

Property	Lower Limit	Upper Limit	Fixed
Radius, r_0(cm)	2	4	
Length, $l = pt$(cm)	0.2	7.2	
Pull rate, p(cm/s)	0.0005	0.003	
Time, t(s)	200	7200	
Melting point, T_f(°C)			1238
Average ambient temperature drop, $T_f - T_a$(°C)	100	300	
Thermal conductivity, $\mathcal{K}$(watts/cm°K)			0.08*
Thermal diffusivity, κ(cm²/s)			0.04
Thermal expansion coefficient, a(°K⁻¹)			1.0×10^{-5}
Elastic stiffnesses, C_{11}(dynes/cm²)			10×10^{11}
C_{12}(dynes/cm²)			4.6×10^{11}
C_{44}(dynes/cm²)			5.1×10^{11}

* Values in column are near T_f.

wall can be written in the condensed form

$$h[\text{cm}^{-1}] = h'\left(\frac{T - T_a}{l}\right)^{1/4} P^{1/2}, \tag{42}$$

where l is the length of the wall, P is the total pressure, and h is a function of the thermal and transport properties of the gaseous ambient and the solid wall. The expression for a liquid medium is similar to eq. (42) with the single exception of taking $P = 1$. A critical evaluation of the constants required to estimate h' will be given elsewhere.[28]

Based on the Stefan-Boltzmann equation for thermal radiation, the coefficient for heat transfer by radiation can be obtained from [16, 18]

$$h[\text{cm}^{-1}] = 5.672 \times 10^{-12}\, \varepsilon\, \frac{(T^4 - T_a^4)}{(T - T_a)\mathscr{K}} \tag{43}$$

where ε and $\mathscr{K}$ are the total emittance and thermal conductivity of GaAs, respectively. We have recently evaluated ε of n-type GaAs as a function of temperature, doping level, and thickness by an analysis of the absorption spectra. For a crystal of 2-cm radius containing 10^{16} cm^{-3} n-type impurities, ε increases from 0.52 to 0.57 in the temperature range between 1200° and 1400°K.[30] If $(T - T_a)$ is not very large, the temperature-dependent term in eq (43) can be given within a good approximation by $4T_a^3$ to yield for h^{16}

$$h[\text{cm}^{-1}] = 0.0227\left(\frac{T_a}{1000°\text{K}}\right)^3 \varepsilon/\mathscr{K}. \tag{44}$$

In Table II, the convective and radiative heat transfer coefficients are summarized at three ambient temperatures. To perform the calculations according to eqs. (42), (43), and (44), we assumed that $(T_f - T)/(T_f - T_a) = 0.7$ and 0.4 for gaseous and liquid or radiative heat transfer, respectively. We can immediately conclude from Table II that in the case of LEC growth for $T_f - T_a \geq 100$, natural convection via the $B_2O_3(l)$ competes with radiative transfer in dissipating the heat from the crystal's external boundaries. This unexpected result is due to the relatively low viscosity of B_2O_3 at these temperatures (100 poise at 1000°C).[31] Hence, convective transfer via the gas phase is nearly negligible in comparison with that by the encapsulating liquid. Furthermore, we find that the approximate eq. (44) for h yields the value of the radiative heat transfer coefficient with adequate precision. Since the convective and radiative heat transfer coefficients are additive, $h \simeq 0.6$ is an appropriate approximate value for LEC growth if $T_f - T_a = 200°$K.

Table II—Convective and radiative heat transfer coefficients at 1 atm

Fluid	h'				l(cm)	h(cm^{-1})		
	at T_f	$T_f - 100°$K	$T_f - 200°$K	$T_f - 300°$K		at $T_f - 100°$K	$T_f - 200°$K	$T_f - 300°$K
$B_2O_3(l)$	0.11	0.089	0.074	0.060	1	0.25	0.24	0.22
$A(g)$	0.0024	0.0023	0.0021	0.0020	4	0.0038	0.0043	0.0045
$N_2(g)$	0.0036	0.0034	0.0032	0.0030	4	0.0057	0.0064	0.0066
$He(g)$	0.0071	0.0068	0.0064	0.0060	4	0.011	0.012	0.013
Radiation								
Exact [eq. (43)]						0.50	0.38	0.28
Approx. [eq. (44)]						0.47	0.34	0.23
Total emittance (10^{16} cm^{-3} n-type, $r_0 = 2$ cm)						0.57	0.55	0.52

4.2 The effect of the variables on the dislocation density

4.2.1 Location and heat transfer coefficient

The effects of axial position and h on the σ_{tot} pattern are illustrated in Figs. 7 and 8, respectively. In view of the fourfold symmetry of the pattern demonstrated in Fig. 6, a polar plot may represent one axial location per quadrant. In Fig. 7, four positions between the top of the crystal and 0.2 cm from the solid-liquid interface are shown, assuming that $h = 0.6$ cm^{-1}, $r_o = 2$ cm, and $p = 0.001$ cm/s and that 5400 seconds have elapsed since the beginning of growth. The numerical labels on all the contours translate immediately into absolute σ_{tot} values if multiplied by $(aE/1 - \nu)[(T_f - T_a)/200]$. Since this convention is observed throughout the paper, the effect of a change in ambient temperature is essentially reflected by a change in $T_f - T_a$.

One can readily conclude from Fig. 7 that at a given time the stress rises from a low value at the top to a maximum at about 0.6 cm from the solid-liquid interface and then diminishes as the interface is ap-
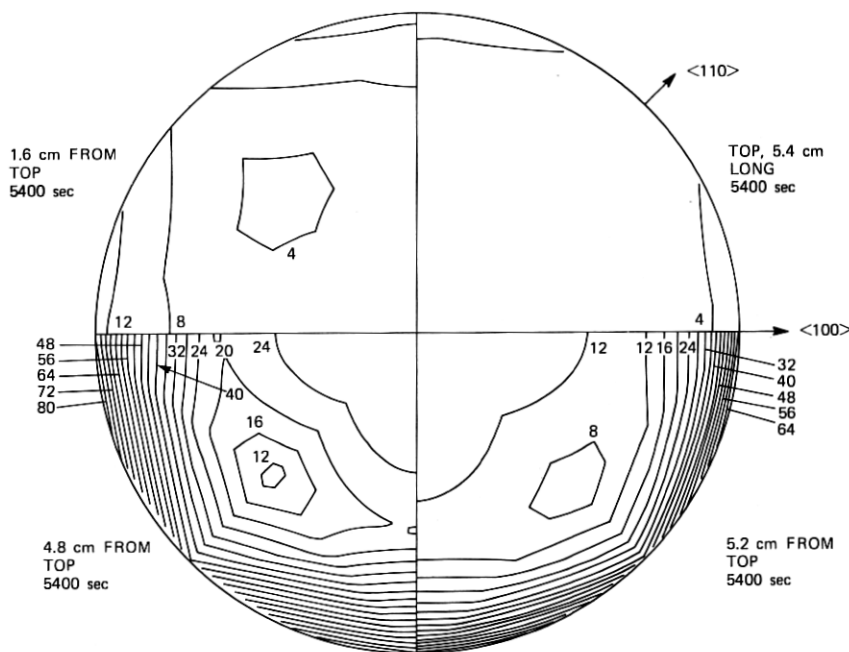

Fig. 7—The axial location dependence of σ_{tot} or dislocation density contour lines for an $\langle 001 \rangle$ GaAs boule at $t = 5400$ s and $h = 0.3$ cm^{-1}. The σ_{tot} levels are labeled, which can be converted into absolute stresses when multiplied by $(aE/1 - \nu)[(T_f - T_a)/200]$. Each successive quadrant in a counterclockwise direction illustrates the dislocation distribution in a wafer at a progressively shorter distance from the solid-liquid interface. The relevant parameters are $p = 0.001$ cm/s, length $= 5.4$ cm, $r_0 = 2$ cm, and $\kappa = 0.04$ cm^2/s.
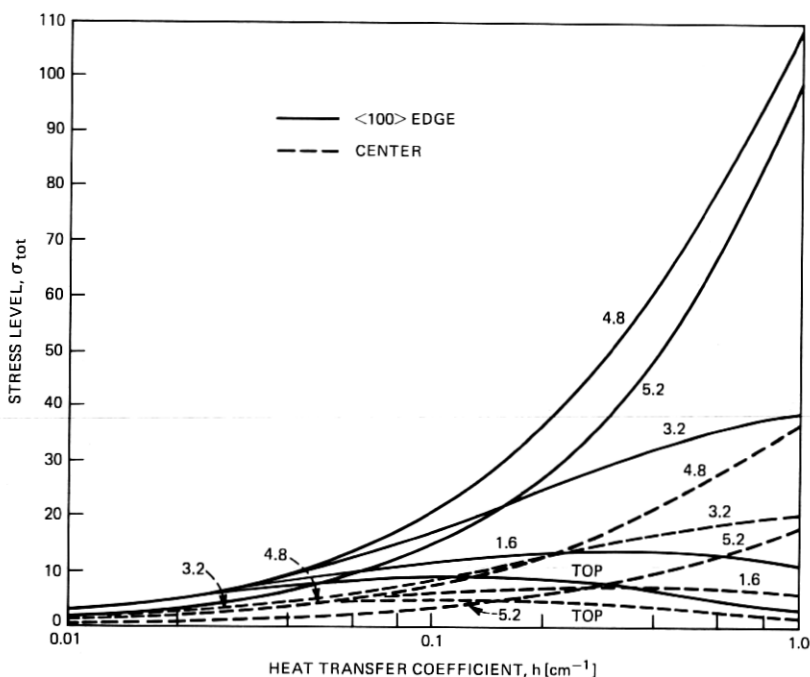
Fig. 8—The dependence of σ_{tot} or dislocation density on the heat transfer coefficient (h) and location ($-z$) for a $\langle 001 \rangle$ GaAs crystal at the center and $\langle 100 \rangle$ edge of a wafer. Absolute stress values can be obtained by multiplying the ordinate with $(aE/1 - \nu)[(T_f - T_a)/200]$. The labels correspond to the distance in centimeters from the top of the crystal. Other key parameters are $t = 5400$ s, length = 5.4 cm, $r_0 = 2$ cm, and $\kappa = 0.04$ cm^2/s. The curves for the center at the top and 1.6 cm from the top, which should be shown merging with the 3.2-cm line at low h values, were terminated at $h \simeq 0.06$ cm^{-1} to reduce crowding.

proached. Moreover, it can be seen that the most severe stress gradient is at the periphery.

In Fig. 8 we show the dependence of σ_{tot} on h at the center as well as at the $\langle 100 \rangle$ edge ($r = 2$ cm, $r_0 = 2$ cm) of a $\{100\}$ wafer. Except for the additional slice at 3.2 cm from the top, the other four locations are the same as in Fig. 7. On the whole, σ_{tot} monotonically rises with h at both the center and edge of the wafer. However, locations in the upper part of the ingot (seed-end) exhibit a maximum at an h value which increases with increasing distance from the top. The simplest mathematical explanation of this result follows from the properties of the term $e^{-\beta_n \psi}$, which plays a prominent role in the limit of large ψ_t and moderate β_n in the expressions for $T - T_a/T_f - T_a$ [eq. (28)] and σ_{tot} [eq. (39) via eq. (32)]. As h becomes larger, so does β_n; hence, for any ψ eventually $e^{-\beta_n \psi} \to 0$. The smaller the value of ψ (the closer the cut to the interface), the bigger the h at which the downturn occurs.

A more physical interpretation of the maximum in the σ_{tot} versus h curves is as follows: The crystal growth model we have been investi-

gating includes two extreme cases. On the one hand, when h is very small, $T - T_a/T_f - T_a \to 1$, because the crystal temperature uniformly approaches that of the molten GaAs(T_f). On the other hand, when h is extremely large $T - T_a/T_f - T_a \to 0$ because the ingot reaches the ambient temperature (T_a) almost instantly. Regardless of the limiting case $[(T - T_a)/(T_f - T_a) = 0$ or $1]$, the thermal stresses must diminish if the crystal temperature is uniform and thus possesses a maximum at an intermediate value of h. Moreover, the temperature at the top of the crystal is closer to T_a than that of the middle. This explains for the same h the tendency of the stress at the top to decrease while at the middle it is still increasing.

Similar to Fig. 7, Fig. 8 also shows the maximum σ_{tot} at 0.6 cm from the solid-liquid interface for both the center and edge of the wafer. At this location, σ_{tot} is a monotonically increasing function of h in a range between 0.01 and 1. Thus the maximum dislocation density is attained at a relatively short distance (say, <1 cm) from the interface. Consequently, by lowering h near the interface, a reduction in dislocation density can be accomplished.

4.2.2 Radius

In Fig. 9, the σ_{tot} contour lines for a crystal with 2-cm radius are superimposed over the lines for one with a 4-cm radius. The other parameters are $h = 0.6$ cm^{-1}, $t = 4500$ s, $p = 0.001$ cm/s, and four locations between the top and 0.5 cm from the interface are given. In general, considering identical locations, the edge of the crystal with a larger radius is more highly stressed than the one with a smaller radius. Comparing equivalent points with the same $\rho = r/r_0$, the effect of increasing the crystal diameter on σ_{tot} appears to be superlinear. However, for cuts near the interface (0.5 cm) the stresses at equivalent points are almost the same. This is a consequence of the fact that, at $\psi = 0.5$ cm, the σ_{tot} of a small diameter crystal just reached its maximum, whereas that of a large diameter crystal is already over its maximum.

To a great extent, the variation of σ_{tot} with r_0 mimics the variation with h (Fig. 8) because the dimensionless quantity $h_1 = r_0 h$ occurs in the key equations. But r_o also appears implicitly in $\psi = (z + pt)/r$. Hence, any h curve family such as Fig. 8 can be used to visualize the effect of increasing the radius provided that appropriate adjustments are made in the h_1 and ψ coordinates. A key finding which is consistent with Fig. 9 is that the larger the diameter of the crystal the farther from the interface is its location of maximum stress.

Although crystals with a larger r_0 are exposed to higher stresses, there is an inherent advantage in growing such crystals if discarding a portion is an acceptable production practice. For example, in the third
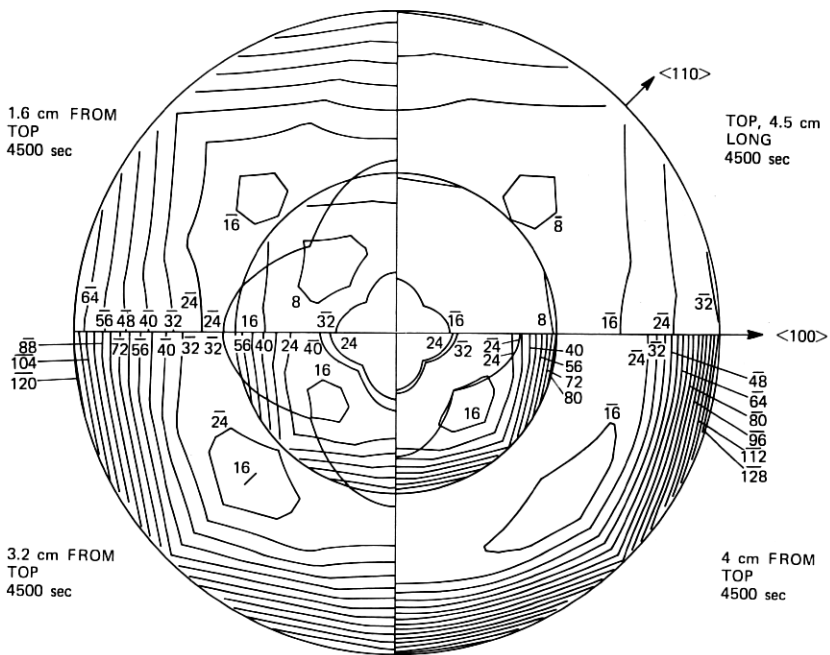
Fig. 9—The dependence of σ_{tot} or dislocation density contours on radius and axial location at 4500 s and $h = 0.6$ cm^{-1}. The inner and outer circles confine the profiles for $r_0 = 2$ and 4 cm, respectively. The labels and labels with bars denote identical stress levels in the GaAs crystal of 2- and 4-cm radius, respectively. Multiplication of the levels by $(aE/1 - \nu)[(T_f - T_a)/200]$ yield the absolute stresses. Each successive quadrant in a counterclockwise direction depicts the dislocation distribution in 2- and 4-cm radius wafers at a progressively shorter distance from the solid-liquid interface. Additional parameters are $p = 0.001$ cm/s, length = 4.5 cm, and $\kappa = 0.04$ cm^2/s.

quadrant of Fig. 9 (3.2 cm from the top), a sizable quasirectangular area of the 4-cm radius crystal is at $\sigma_{\text{tot}} \leq 56$. In the case of the 2-cm radius crystal, almost the entire area is at a comparable level or less. If level 56 were below the threshold stress for slip, then there would be an approximately 2:1 gain in area yield in cutting out a rectangular portion of the larger diameter wafer over keeping the entire area of the smaller diameter one. Since we have found that the stresses in the slender ingot would further increase down to a distance of $\simeq 0.5$ cm from the interface (fourth quadrant), the choice to cut a sizable area, low in defect density, from the broader ingot is even more favorable.

4.2.3 Time

Time is an implicit variable in the quasi-steady-state temperature and stress profile equations. In the preceding parts of this section, the stress levels were given at various axial locations, subsequent to the growth of a GaAs ingot for a fixed length of time. In Fig. 10, we present polar plots of the σ_{tot} contours which prevail at the top of the crystal—
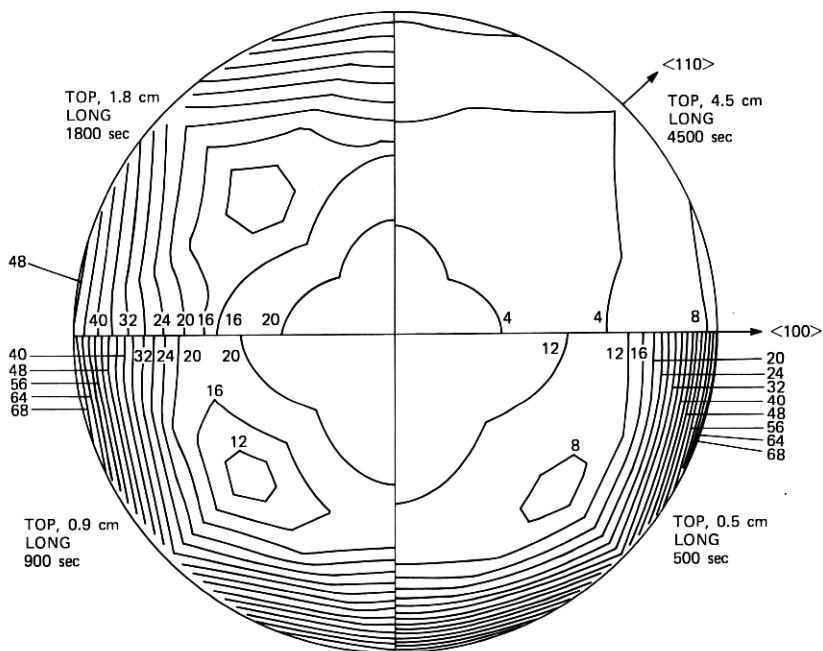
Fig. 10—The time dependence of the σ_{tot} or dislocation density contours of a GaAs boule at $h = 0.6$ cm^{-1}. Starting in the fourth quadrant and proceeding in a clockwise direction, the time evolution of the dislocation pattern at the top end of a growing crystal is shown. The labels correspond to the stress levels and are converted into absolute values when multiplied by $(aE/1 - \nu)/[(T_f - T_a)/200]$. Other relevant parameters are $p = 0.001$ cm/s and $r_0 = 2$ cm.

a fixed location—after 500, 900, 1800, and 4500 seconds of growth. The other key parameters are $h = 0.6$ cm^{-1}, $r_0 = 2$ cm, and $p = 0.001$ cm/s. One can readily see that, as crystal growth proceeds, the top is exposed very early to the maximum stress, namely between 500 and 900 seconds.* Afterwards, the stress levels rapidly decline in magnitude. It is apparent that the patterns at a fixed location but for different durations of growth (Fig. 10) parallel the ones at a set time but for different axial locations (Fig. 7, Fig. 9, $r_0 = 2$ cm). Intuitively, this should not be surprising. For instance, after 4500 s, the top is 4.5 cm from the solid-liquid interface and a segment of the crystal is at a distance of, say, 0.5 cm from the interface. Then the pattern at the latter position may resemble that of the top at 500 s, at which time the boule was only 0.5 cm long. Formally, the time-location equivalence is only exact when $e^{-\beta_n \psi}$ is a very good approximation of the axial function in eq. (28). Otherwise, it indicates a useful trend in correlating time and position variations.

---

* Compare Fig. 10, quadrants 3 (900 s) and 4 (500 s) near the center.

By concentrating on a single point at the top, a more complete representation of σ_{tot} can be provided than has been achieved by the polar plots alone in Fig. 10. We show in Fig. 11 σ_{tot} as a function of time at the top $\langle 100 \rangle$ edge of a GaAs ingot. A family of these curves with h varying between 0.01 and 2 cm^{-1} is given. Each member of the family exhibits a maximum in σ_{tot} at a critical time, t_c. More effective heat transfer in the growth system leads to an earlier t_c and to a larger and steeper maximum in σ_{tot}. As already mentioned with respect to
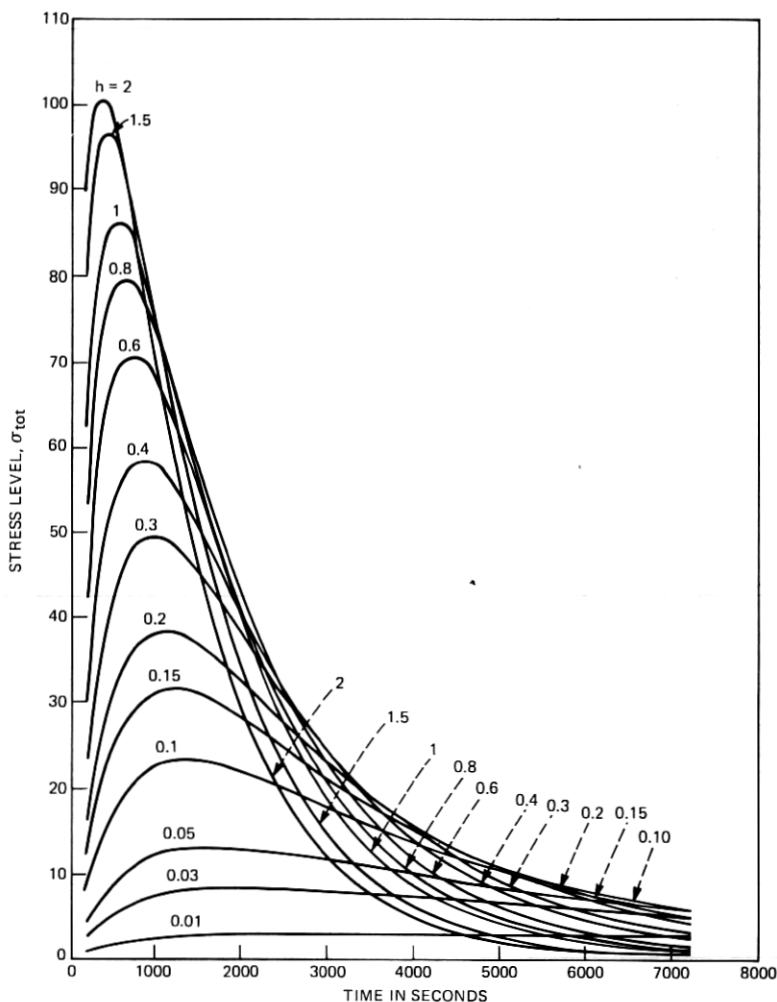

Fig. 11—The variation of σ_{tot} or dislocation density with time and heat transfer coefficient (h) at the top $\langle 100 \rangle$ edge of a GaAs crystal. The labels are the heat transfer coefficients in cm^{-1}. Multiplication of the stress levels by $(aE/1 - \nu)[(T_f - T_a)/200]$ yields the absolute value of the stresses. The other parameters are $p = 0.001$ cm/s, $r_0 = 2$ cm, and $\kappa = 0.04$ cm^2/s.

Fig. 8, it can also be seen in Fig. 10 that as $h \to 0$ and ∞, $\sigma_{\text{tot}} \to 0$ because the temperature of the crystal approaches uniformly the constant values T_f and T_a, respectively.

If $h = 0.6$ cm^{-1}, the maximum in σ_{tot} at the top $\langle 100 \rangle$ edge of GaAs is at ~700 s. As the crystal grows longer, the size of the stress diminishes. Thus, the time-dependence study confirms the conclusion that the maximum dislocation density is attained during the early phase of growth. Of course, it is presupposed here that the dislocations form instantaneously when the stress is above the critical resolved shear stress and that the density of dislocations thus frozen-in irreversibly will not be reduced by the drop in the stress level as the crystal grows longer. A downward adjustment of h is the most obvious method by means of which the dislocation density is reducible.

4.2.4 Pull rate

Figure 12 presents a composite set of polar plots to demonstrate the effect of pull rate on σ_{tot}. The left and right halves show the results for
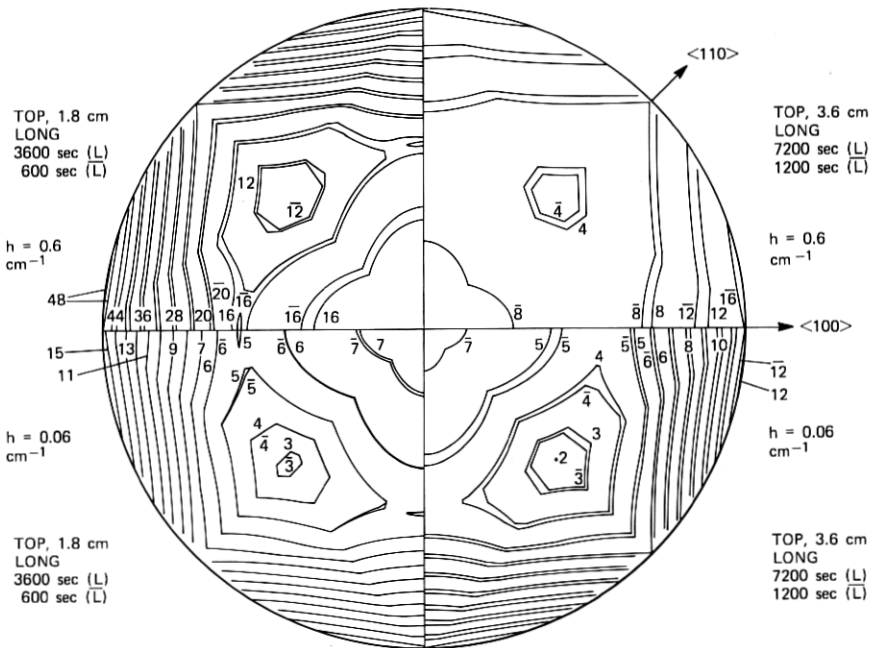

Fig. 12—The effect of pull rate (p) on the σ_{tot} or dislocation density contours at the top of a GaAs boule. The labels and labels with bars (space permitting) denote identical stress levels at $p = 0.0005$ and 0.003 cm/s, respectively. Multiplication of the levels by $(aE/1 - \nu)[(T_f - T_a)/200]$ provides the absolute stresses. The two quadrants in the upper and lower halves show the patterns at $h = 0.6$ and 0.06 cm^{-1}, respectively. The two quadrants in the left and right halves illustrate the distribution at the top of a 1.8- and 3.6-cm long crystal, respectively. Since the lengths are constant, the times for growth are consistent with the selected pull rates. Other parameters of interest are $r_0 = 2$ cm and $\kappa = 0.04$ cm^2/s.

the top of a 1.8- and 3.6-cm long ingot, respectively, while the top and bottom halves represent the profiles at $h = 0.6$ and 0.06 cm^{-1}, respectively. The other parameters are $r_o = 2$ cm and $p = 5 \times 10^{-4}$ and 3×10^{-3} cm/s. The fixed lengths correspond to growth times $t = 3600$ s and 600 s for $p = 5 \times 10^{-4}$ and 3×10^{-3} cm/s, respectively, for the 1.8-cm long ingot. When the length is 3.6 cm, the times are doubled. As one would expect from the analytical expressions and as also seen in Fig. 12, the influence of a sixfold increase of pull rate on the dislocation distribution is more pronounced in the case of a longer boule than that of a shorter one.

To provide a more precise discussion with reference to the effect of pull rate on σ_{tot}, an approximate expression will be derived for the fractional increase of σ_{tot} at the top $\langle 100 \rangle$ edge as p changes. The calculation can be performed solely by means of eq. (32b) since at the $\langle 100 \rangle$ edge $\sigma_{tot} = (8\sqrt{6}/6)\sigma_\theta$. Then, in view of the fact that p_1 is more effective in modifying h_p than β_n,* one finds for the relative change in σ_{tot}, $(\sigma''_{tot} - \sigma'_{tot})/\sigma'_{tot'}$, taking only the leading term in the series of eq. (32b),

$$\frac{\sigma''_{tot} - \sigma'_{tot}}{\sigma'_{tot}}$$

$$\simeq (p''_1 - p'_1)\frac{l}{2r_0}\left[1 - \frac{1 - e^{-2\beta_1 l/r_0}}{l/r_0[h''_p + \beta_1 - (h''_p - \beta_1)e^{-2\beta_1 l/r_0}]}\right], \quad (45)$$

where the double and single primes refer to faster and slower pull rates, respectively, and l is the length of the crystal. At a reasonably rapid h, eq. (45) reduces to

$$\frac{\sigma''_{tot} - \sigma'_{tot}}{\sigma'_{tot}} \simeq (p''_1 - p'_1)\frac{l}{2r_0}\left(1 - \frac{1}{\frac{l}{r_0}(h''_p + \beta_1)}\right) \quad (46)$$

since the exponentials approach zero. For very small h_1, a Taylor series expansion of the exponentials yields

$$\frac{\sigma''_{tot} - \sigma'_{tot}}{\sigma'_{tot}} \simeq (p''_1 - p'_1)\frac{l}{2r_0}\left(1 - \frac{1}{1 + \frac{l}{r_0}(h''_p - \beta_1)}\right). \quad (47)$$

According to eq. (45), the effect of stress can be readily observed for a long crystal if the difference in pull rates is large. If the heat transfer coefficient is substantial, the full impact of the growth rate term $e^{p_1\psi/2}$ in eq. (32b) is achieved because the multiplier $1 - [1/l/r_0(h''_p +$

* Eqs. (29) show that β_n is relatively insensitive to a change in p_1 on account of its dependence on $p_1^2/2$.

$\beta_1)] \to 1$ [eq. (46)]. On the other hand, if h is minute the multiplier approaches zero [eq. (47)] and the dependence of σ_{tot} on pull rate, especially for short l, is negligible. The stress patterns in the top two quadrants ($h = 0.6$) and bottom two quadrants ($h = 0.06$) of Fig. 12 fully demonstrate the validity of these general remarks.

It is apparent that, of all the parameters here considered, a change in pull rate is perhaps the least effective method by which one may influence the stress levels in GaAs. As can be most readily observed in the first quadrant of Fig. 12, for identical spots the wafer sliced from an ingot grown at a slower pull rate is under less stress than the one obtained at a faster pull rate. This can be rationalized by noting that the key quantity h_p is the sum of h_1 and $p_1/2$. In essence, a more rapid p_1 is analogous to an increase in h_1; hence, the greater p_1, the steeper the temperature gradient from axis to edge and the larger the thermal stresses. Although the effect of pull rate on the stress pattern is relatively small, if on account of other factors the resolved shear stress happens to be only marginally higher than its critical value, it may become feasible to reduce the dislocation density by lowering the pull rate.

4.3 Comparison with experiment

In Fig. 13 a macrophotograph of a {100} wafer cut from the vicinity of the seed or top-end of a Te-doped GaAs boule is presented. To reveal the dislocation structure, the wafer was etched in fused KOH at 300°C for 1 hour. It has been previously reported by Angilello et al[32] that, on a {100} wafer of GaAs, there is a one-to-one correspondence between the dislocation density determined by X-ray transmission topography and the pits decorated by the etchant where the dislocations intersect the surface. The dislocation density in Fig. 13 varies between 10^4 and $5 \times 10^4/\text{cm}^2$.

A microscopic view of the dislocation distribution for a Cr-doped {100} wafer is given in Fig. 14. This composite picture clearly illustrates the dislocation density in four critical regions of an etched GaAs slice. One can readily discern the following key features of the dislocation distribution:

(*i*) Fourfold symmetry.

(*ii*) Maximum density at the $\langle 100 \rangle$ edge.

(*iii*) Minimum density midway between center and $\langle 110 \rangle$ edge.

(*iv*) Intermediate densities at center and $\langle 110 \rangle$ edge, but the edge density is somewhat higher.

In fact, all the calculated σ_{tot} contour lines possess the preceding characteristics. To make the comparison more convenient, we have replotted the polar diagram of Fig. 6 in the form of a "gray scale" in Fig. 15. Accordingly, increasing stress levels in Fig. 6 correspond to
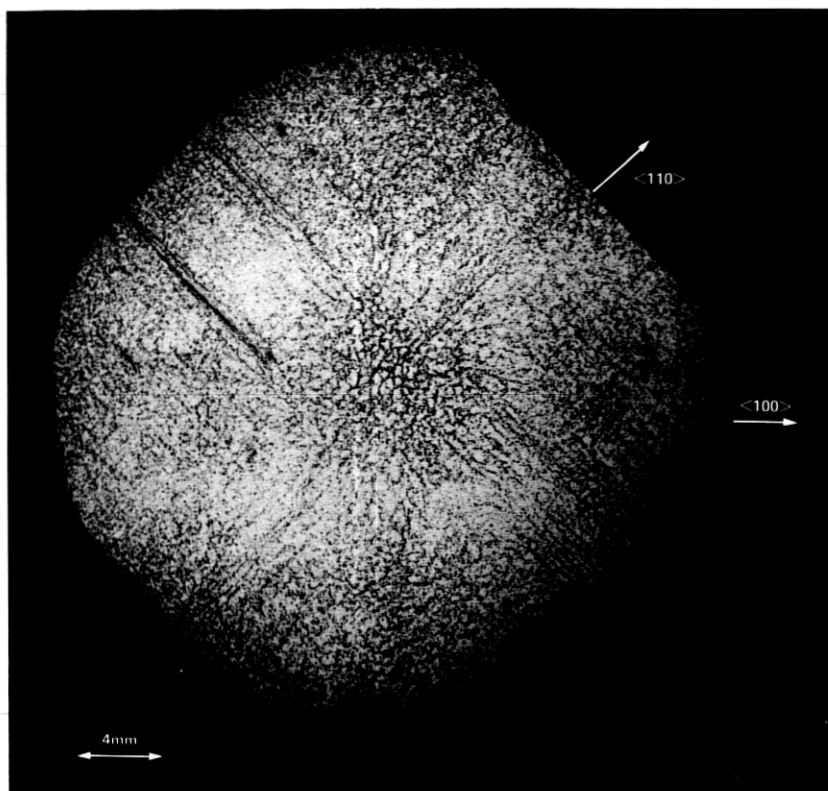
Fig. 13—Macrophotograph at ~5X magnification of a KOH-etched {001} GaAs wafer. The crystal was cut from the vicinity of the top-end of a Te-doped GaAs boule grown by the LEC technique.

more darkly shaded areas in Fig. 15, in the manner of a geographic contour map. The agreement between the experimental results and the theoretical prediction is very good.

The observed symmetric pattern in Figs. 13 and 14 is not dependent on the type of dopant incorporated in GaAs in view of the similar distribution of dislocations found in chromium as well as tellurium-doped samples. However, the farther away the cut from the top of the ingot the more diffuse the distribution. This is not surprising if account is taken of the tendency of dislocations to move out of their slip planes by climb. Morever, the typical 60-degree dislocations[33] generated at the top by thermal stress-induced glide continue into the next-to-grow layer of the crystal and add to the glide dislocations arising therein. Therefore, extra mechanisms notwithstanding, the progenitor of dislocations in GaAs is crystallographic glide relieving the severe thermal stresses associated with the Czochralski growth process.
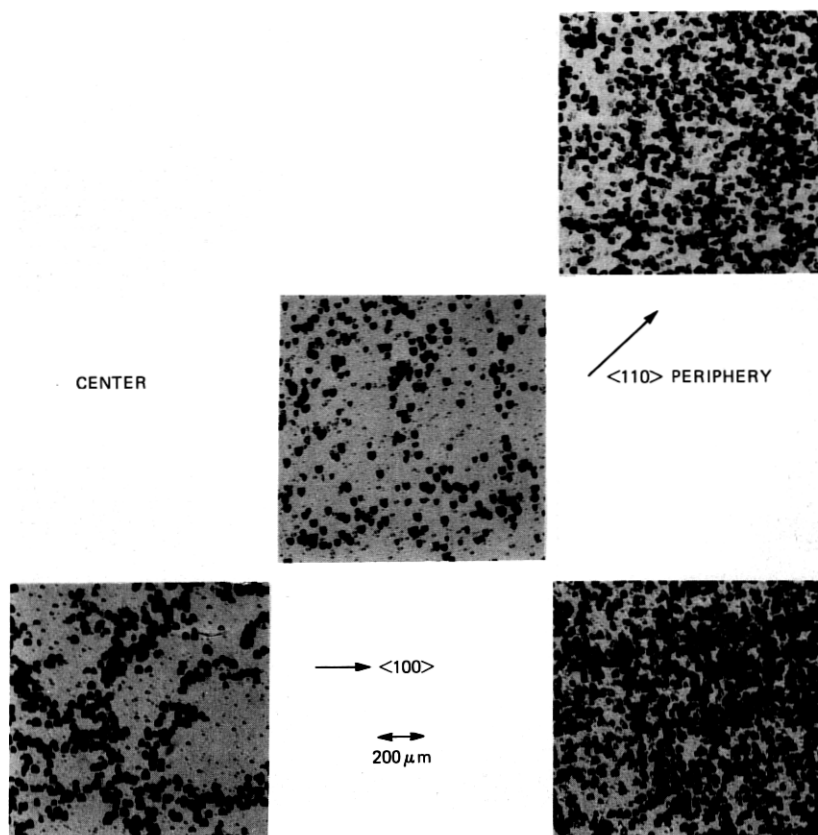
Fig. 14—Photomicrographs of important regions within a KOH-etched {001} GaAs wafer. The crystal was cut from the vicinity of the top-end of a Cr-doped GaAs ingot grown by the LEC technique. The original locations are indicated in a realistic though schematic fashion.

4.4 Estimation of the critical stress level

Having correlated the empirical dislocation density pattern of a {100} GaAs wafer with the total resolved shear stress profile, σ_{tot}, the critical value of this quantity at which slip is initiated becomes a topic of preponderant interest. It has been previously stated that in all diagrams multiplication of the stress level by $(aE/1 - \nu)[(T_f - T_a)/200]$ yields the stress in absolute units (dynes/cm^2). Although the original stress equations are those of isotropic thermoelasticity, by a minor modification of the constant $E/1 - \nu$ it is possible to take into account to some degree the anisotropy of the cubic GaAs. According to Brantley, for stresses acting in directions within {111} planes $E/1 - \nu$ is an invariant quantity.[34] Since the GaAs slip system is {111}, $\langle 1\bar{1}0 \rangle$, it is reasonable to employ $(E/1 - \nu)_{\{111\}}$ in our estimates. Based
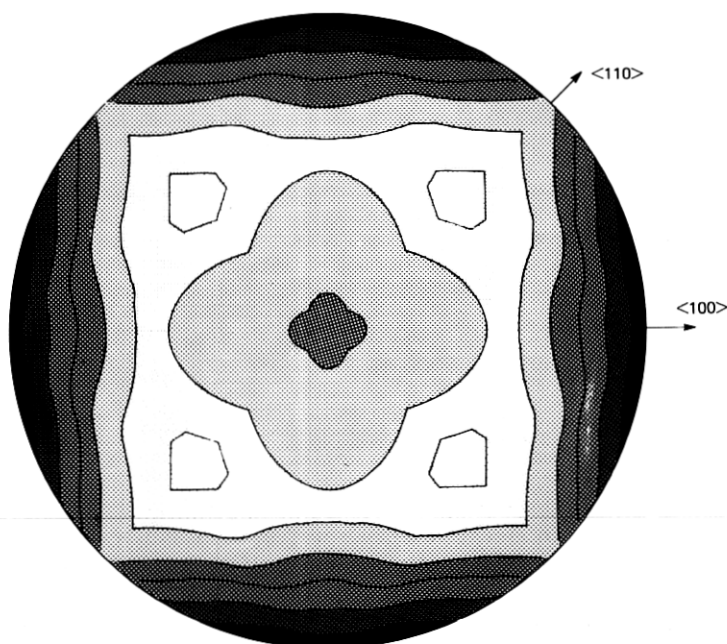
Fig. 15—"Gray scale" representation of the constant σ_{tot} or dislocation density contour lines for the top wafer of a $\langle 001 \rangle$ GaAs boule. The shading is based on the pattern in Fig. 6.

on Brantley's work we can write

$$\left(\frac{E}{1-\nu}\right)_{\{111\}} = \frac{1}{\mathscr{S}_{11} + \mathscr{S}_{12} - \mathscr{S}/3} \tag{48a}$$

or

$$\left(\frac{E}{1-\nu}\right)_{\{111\}} = C_{11} + C_{12} + \frac{C(C_{11} + 4C_{12}) - 3C_{12}^2}{2C + 1.5C_{11}}, \tag{48b}$$

depending on whether one uses elastic stiffnesses (C_{ij}) or compliances ($\mathscr{S}_{ij}$). The symbols $\mathscr{S}$ and C represent the departures from isotropy and are given by $\mathscr{S} = \mathscr{S}_{11} - \mathscr{S}_{12} - \frac{1}{2}\mathscr{S}_{44}$, $C = C_{44} - \frac{1}{2}(C_{11} - C_{12})$. If $\mathscr{S} = C = 0$, the crystal is isotropic.

Table III lists the expansion coefficient, $(aE/1-\nu)_{\{111\}}$, $(aE/1-\nu)_{\text{isotropic}}$ for GaAs at various temperatures. The data sources and their critical evaluation will be given elsewhere.[28] Obviously, the product of $(T_f - T_a)/200$ times the tabulated value times the stress level given in the various figures provides the absolute stress.

The critical resolved shear stress (CRSS) of GaAs between 250° and 550°C has been determined by Swaminathan and Copley.[35] To extrap-

DISLOCATION GENERATION IN GaAs CRYSTALS **629**

Table III—Some elastic properties of GaAs

Temperature (°K)	T_f	$T_f - 100°K$	$T_f - 200°K$	$T_f - 300°K$	298°K
$a \times 10^{-6}(°K^{-1})$	10.4	10.1	9.69	9.31	5.80
$\left(\dfrac{aE}{1-\nu}\right)_{(111)} \times 10^7(\text{dynes/cm}^2°\text{K})$	1.55	1.51	1.48	1.44	1.01
$\left(\dfrac{aE}{1-\nu}\right)_{iso} \times 10^7(\text{dynes/cm}^2°\text{K})$	1.10	1.07	1.05	1.02	0.72
$1.2 \times \left(\dfrac{aE}{1-\nu}\right)_{iso} \times 10^7(\text{dynes/cm}^2°\text{K})$ [anisotropic coefficient]	1.32	1.28	1.26	1.22	0.86
$8 \times \text{CRSS} \times 10^7(\text{dynes/cm}^2)$,	4.5	5.2	6.2	7.5	

olate their results to elevated temperatures, we assumed, as is usual,[25] that the CRSS is an exponential function of reciprocal temperature. Table III also lists CRSS multiplied by 8, which we call the effective CRSS. The factor 8 is used to facilitate comparison with σ_{tot} because at the $\langle 100 \rangle$ edge of a $\{100\}$ wafer 8 slips of identical magnitude operate $[\sigma_{tot} = 8\sqrt{6}/6\sigma_\theta]$.

Let us compare Fig. 11 with the values in the $T_f - 200°C$ column in Table III. It can be seen that even for level 5 $\sigma_{tot} = 5 \times 1.5 \times 10^7 = 7.5 \times 10^7$ dynes/cm^2 is larger than the effective CRSS of 6.2×10^7 dynes/cm^2. Therefore, if the plotted level is above 4.1, the $\langle 100 \rangle$ edge of the top will develop dislocations at ~1000 s. This corresponds to a threshold of $h = 0.02$ in Fig. 11. In other words, if $h < 0.02$ cm^{-1} dislocations cannot be avoided in GaAs at least at the $\langle 100 \rangle$ edge of a 4-cm diameter $\{100\}$ wafer. At $h = 0.6$ cm^{-1} which is the heat transfer coefficient appropriate for LEC growth, the estimated σ_{tot} variation in the $\langle 110 \rangle$ direction is ~21, 12, and 54×10^7 dynes/cm^2 from the center through a midway point, and the periphery, respectively (Fig. 10, fourth quadrant). At the $\langle 100 \rangle$ edge $\sigma_{tot} = 105 \times 10^7$ dynes/cm^2 (Fig. 11). Although all these values are above the effective CRSS, one should be aware of the errors involved in the various estimates and realize that it may be relatively easy to achieve a nearly dislocation-free material near the $\langle 110 \rangle$ midway spot (12 vs 105×10^7 dynes/cm^2). Therefore, by judicious design changes to decrease $T_f - T_a$, h and p which are associated with the Czochralski growth process of GaAs, at least the reduction, if not the elimination, of dislocations is a realistic possibility. Since the dislocation density gradient is the steepest near the periphery, even improvements in the inner two-thirds of the wafer area could be of practical benefit.

4.5 The effect of anisotropy

To calculate σ_{tot}, we adjusted the isotropic thermal stress equation by using an invariant value of $E/1 - \nu$ valid for stress directions within {111} planes.[34] Strictly speaking, this is not identical with finding a true anisotropic solution for the thermal stresses arising during Czochralski growth. Even under isothermal conditions, to solve the equations of elasticity for an anisotropic body is a formidable undertaking.[36] Only in the case of a simple temperature profile is there any hope to obtain in a closed form the thermal stresses acting on an anisotropic cylinder. This can be most clearly seen by inspecting the partial differential equation of thermoelasticity for a cubic crystal with a $\langle 100 \rangle$ axis, in the so-called stress formulation. Following the derivation outlined by Boley and Weiner[37] for plane strain in an isotropic body, we find for cubic material

$$\nabla^2(\sigma_x + \sigma_y) - \frac{\mathcal{S}_{11}\mathcal{S}}{\mathcal{S}_{11}^2 - \mathcal{S}_{12}^2}\left(\frac{\partial^2\sigma_x}{\partial x^2} + \frac{\partial^2\sigma_y}{\partial y^2}\right) = -\frac{a\nabla^2 T}{\mathcal{S}_{11} + \mathcal{S}_{12}}, \qquad (49)$$

where ∇^2 is the Laplacean operator in Cartesian coordinates. If $\mathcal{S} = 0$, the partial differential equation is that of an isotropic body and the complication due to the inclusion of the second term on the left-hand side of eq. (49) disappears. Grechushnikov and Brodovskii[38] succeeded in solving eq. (49) for a quenched cubic cylinder with a $\langle 100 \rangle$ axis by assuming a radially parabolic temperature profile taken from the early heat transfer studies of Adams and Williamson.[39]

Based on the work of Grechushnikov and Brodovskii,[38] we can evaluate the ratio $\sigma_\theta(\text{anisotropic})/\sigma_\theta(\text{isotropic})$ in the form

$$\frac{\sigma_\theta(\text{anisotropic})}{\sigma_\theta(\text{isotropic})} = \frac{1}{1 - [\mathcal{S}_{11}\mathcal{S}/4(\mathcal{S}_{11}^2 - \mathcal{S}_{12}^2)]} \qquad (50)$$

and substituting the appropriate values

$$\sigma_\theta(\text{anisotropic}) \simeq 1.2\sigma_\theta(\text{isotropic}).$$

Since at the $\langle 100 \rangle$ edge of a crystal $\sigma_{tot} = 8(\sqrt{6}/6)\sigma_\theta$, multiplication of the values in the values in the third column in Table III [$(aE/1 - \nu)_{iso}$] by 1.20 could serve as a suitable estimate of the effect of anisotropy on σ_{tot}. As shown in Table III, the anisotropic coefficient lies between the $(aE/1 - \nu)_{\{111\}}$ and $(aE/1 - \nu)_{iso}$ results. In practical terms, this means that the threshold level rises from 4.1 to 4.9 if the anisotropic coefficient instead of $(aE/1 - \nu)_{\{111\}}$ is used. This is indeed a minor perturbation and the conclusions of this study are not influenced by the anisotropic solution.

4.6 Additional characteristics of the quasi-steady-state solution

The temperature profiles prevailing during Czochralski growth [eq. (28)] were based on the quasi-steady differential equation [eq. (5)] which depends explicitly on pull rate and implicitly on time, via ψ and ψ_t [eqs. (29)]. Since T_a was taken as a constant, in the limit of $p \to 0$, the QSS solution reduces to the steady-state result of Brice[14]/Carslaw and Jaeger.[16] To gain insight into the degree of approximation involved in using the QSS instead of a true time-dependent solution of eq. (4) when determining the temperature distribution, we have examined the departure from equality of eq. (4) by substituting T from eq. (28). Having performed the indicated operations, we conclude that at the top-end of the crystal the QSS solution satisfies eq. (4) if and only if $\exp(p_1/2 - \beta_n)pt/r_0$ approaches zero. Since, in general, $p_1/2 < \beta_n$, this finding suggests that a moderate pull rate, efficient heat transfer into the ambient medium, and a reasonable passage of time since the inception of growth are the conditions at which the QSS solution is the most satisfactory.

Not only mathematical but also conceptual difficulties are associated with a search for a true transient solution to Czochralski growth. In classical heat transfer (or diffusion) problems, a physical body exists initially ($t = 0$) with given properties (prescribed temperatures or fluxes). In contrast, in crystal growth, the initial state is that of a liquid from which the solid materializes by phase transformation at $t > 0$. Hence, the boundary conditions for the crystal [e.g., eqs. (15) and (16)] have no initial relevance.

Strictly speaking, heat transfer during crystal growth belongs to the group of problems involving a change of state which is often referred to as "Stefan's problem." According to Carslaw and Jaeger,[16] the few existing exact solutions of "Stefan's problem" pertain to very simple boundary conditions and semi-infinite geometries. A typical illustrative example is as follows: Suppose a liquid column at T_f is contained in a very wide and tall crucible. Then, beginning at $t > 0$ the temperature at the bottom is lowered to a fixed value below T_f and, consequently, a freezing front moves upwards. Clearly, each region must satisfy the one-dimensional partial differential equation of heat conduction and the temperatures are equal at the solid-liquid interface (T_f). In addition, if the density of the two phases is nearly equal, the heat-flux balance at the interface demands that

$$\mathcal{K}_c \frac{\partial T_c}{\partial s} = \mathcal{K}_l \frac{\partial T_l}{\partial s} + \frac{\Delta H_f}{V_m} \frac{ds}{dt}, \qquad (51)$$

where s is the distance from the bottom and $\mathcal{K}_i(i = \text{crystal or liquid})$, ΔH_f, and V_m denote the thermal conductivity, heat of fusion, and molar volume, respectively. In spite of the nonlinear boundary condi-

tion [eq. (51)], Neumann succeeded in determining the exact vertical temperature profile in both phases and the location of the interface as a function of time in terms of error functions.[16]

Currently, more sophisticated situations such as a body of finite length can be treated by Boley's "embedding technique" which involves an imaginary extension of the solid and liquid phases into the space actually occupied by the diminishing liquid and growing solid fronts, respectively.[40] Although this technique circumvents the conflict between the boundary and initial conditions, it leads to a complicated integro-differential equation which is only amenable to a series solution.

Therefore, it is apparent that only by overcoming the severe conceptual and analytical obstacles can one attain a more realistic description of the Czochralski growth process especially in the vicinity of the solid-liquid interface and at the beginning of crystallization. In particular, if the effect of the physical and geometrical conditions on the interface shape is a matter of preponderant interest, a numerical finite-difference solution of the appropriate heat transfer equation[41] is likely to be unavoidable.

As a reasonable approximation for GaAs under the prevailing Czochralski growth conditions, it has been assumed in the QSS model that at the interface $(\psi = s/r_0 = 0) T = T_f$. Below T_f in the crystal the QSS isotherms $[\psi = f(\rho, T = \text{constant})]$ are all concave with a maximum at $\rho = 0$. Essentially, the isotherms mimic the complement of the temperature profiles in Fig. 3 $[1 - (T_f - T)/(T_f - T_a)]$. Of course, at the interface a flux balance of the type given in eq. (51) must be obeyed. In general, depending on whether the temperature of the liquid nutrient is higher or lower than on the axis at T_f, a convex or concave interface, respectively, results.[42] However, it can be demonstrated with respect to the QSS calculations here considered that the assumption of a planar isotherm at T_f is internally consistent. Let us evaluate the heat flux according to eq. (51). Then, taking $\partial T_1/\partial s = 0$ and identifying $ds/dt = p$,

$$\mathscr{K}_c \frac{\partial T_c}{\partial s} = p \frac{\Delta H_f}{V_m} = -3.7 \text{ watts/cm}^2. \tag{52}$$

Differentiating eq. (28) and substituting the appropriate parametric values,* we find the fluxes at 0.4 cm from the solid-liquid interface and at the interface at selected values of h as shown in Table IV. The listed results clearly indicate that if $h \simeq 0.1$ or less, nearly planar interface can be maintained; moreover, the heat of crystallization is readily

---

* $\Delta H_f = 25.080$ kcal/gmole,[43] $\rho = 5.16$ g/cm^{3}[44], $t = 3600$ s, length $= 3.6$ cm, $p = 0.001$ cm/s, $r_0 = 2$ cm, $\mathscr{K} = 0.08$ watts/cm°K, $\kappa = 0.04$ cm^2/s, $T_f - T_a = 200$°K.

Table IV

$h[\text{cm}^{-1}]$	$\mathscr{K}_c\dfrac{\partial T_c}{\partial s}$ [watts/cm^2]	
	3.2 cm from top axis/edge	3.6 cm from top axis/edge (interface)
0.03	−1.8/−2.2	−1.8/−3.4
0.10	−4.0/−5.1	−4.1/−9.2
0.30	−6.7/−8.9	−7.1/−20.1

dissipated if $h \gtrsim 0.1$. It should be emphasized that irrespective of the shape of the melting point isotherm, its effect on the temperature distribution at some distance from the interface—where the maximum in σ_{tot} and the dislocation density occurs—is not expected to be significant.

An additional feature of the QSS model is that the more effective the convective heat transfer, the more concave the isotherm. The partial derivatives of T obey the relationship

$$\left(\frac{\partial s}{\partial \rho}\right)_T = \frac{-(\partial T/\partial \rho)_s}{(\partial T/\partial s)_\rho} \tag{53}$$

at any isotherm. Evaluating eq. (53) by means of information such as given in Fig. 3 and Table IV, we find at 0.4 cm from the interface and at $\rho = 1$

$h[\text{cm}^{-1}]$	$\left(\dfrac{\partial s}{\partial \rho}\right)_T$ [cm]
0.1	−6.9
0.3	−9.3

Obviously, the more negative tangent at $h = 0.3$ corresponds to a more concave isotherm.

V. SUMMARY AND RECOMMENDATIONS

We have determined the temperature distribution arising during the Czochralski growth of GaAs by solving the quasi-steady-state partial differential equation for heat conduction. The solution includes time, radius, axial location, pull rate, a constant ambient temperature, and heat transfer coefficient among the variables and permits the assessment of their effect. The temperature profiles enabled us to calculate the radial, tangential, and axial thermal stresses in the growing cylindrical boule in a closed form. These stresses were required to evaluate the sum of the absolute values of the 12 resolved shear stress components (σ_{tot}) appropriate for the $\{111\}$, $\langle 1\bar{1}0 \rangle$ slip system. It was postu-

lated that in the case of complete stress relief σ_{tot} is proportional to the dislocation density within an additive constant. To directly relate the model calculations to actual sample geometry, we have generated constant σ_{tot} or dislocation density contour lines for a circular {100} wafer. The dislocation pattern has fourfold symmetry. An absolute minimum in density is found in the $\langle 110 \rangle$ direction at ~0.6x wafer radius. The center and edge of the wafer are heavily dislocated, the density being largest at the edge. The calculated patterns are in accord with KOH-etched dislocation patterns on wafers cut from near the top end of Cr- and Te-doped GaAs ingots, strongly suggesting that the original source of dislocations is crystallographic glide induced by the excessive thermal stresses associated with crystal growth.

By a variation of the parameters, we have reached the following conclusions:

(*i*) Doubling the radius (2 to 4 cm) of the ingot more than doubles the dislocation density. However, for comparable densities, the larger diameter wafer has a useful area in excess of the entire area of the smaller diameter one.

(*ii*) Reducing the pull rate by a factor of 6 (10.8 cm/h to 1.8 cm/h) has only a small effect on reducing the dislocation density.

(*iii*) Dislocations near the top of the ingot are grown-in by the time the ingot is less than 1 cm long (i.e., σ_{tot} is at its time-dependent maximum).

(*iv*) The more effective the convective and radiative heat transfer from the surface of the boule, the larger σ_{tot} and the dislocation density. In the case of LEC growth, natural convection ($h = 0.24$ cm^{-1}) and radiation ($h = 0.34$ cm^{-1}) through the ~1-cm long B_2O_3 column are the predominant heat transfer mechanisms. For Czochralski growth with a gaseous ambient, h is only about 2 to 4 percent of that for B_2O_3.

(*v*) Using extrapolated values of the measured elastic constants, thermal expansion coefficient and critical resolved shear stress in combination with the model calculations, we find that dislocations can be avoided if the approximate inequality $(T_f - T_a) h \lesssim 4°K/cm$ holds. For $(T_f - T_a) = 200°K$, h should be less than 0.02 cm^{-1}. Therefore, it is not surprising that the LEC growth of GaAs ($h \approx 0.6$) leads to significant dislocation generation. Although, in practice, h cannot be readily decreased below 0.02 cm^{-1}, any reduction in h and/or $T_f - T_a$ will result in a proportional reduction in dislocation density.

Some of these conclusions appear to be consistent with the experience of Leung and Allred[45] who reported on a liquid seal growth technique for GaAs. In this method, B_2O_3 is located at the growth chamber pull-rod junction. The chamber is filled with excess As_2 and a resistance-wound after-heater over the ingot is employed. That this technique provides, as reported, low-dislocation density crystals is reasonable in view of the quasi-steady-state model. Accordingly, based

on molecular weight considerations h for As_2 is very small (must be below that for A in Table II), convection through B_2O_3 is avoided, and $(T_f - T_a)$ is reduced by means of the after-heater. However, for routine growth of GaAs, the above method is impractical.

Clearly, there are several areas to focus on in the case of LEC growth. The thinnest possible B_2O_3 layer consistent with preventing As escape should help limit the large connective transfer well before the dislocations reach their maximum density. Radiation shields will lower the radiative heat transfer coefficient and after-heaters may be used to increase T_a. Moreover, on large area wafers, the high dislocation density periphery may be removed following growth. In any event, an empirical balance must always be struck between reducing the dislocation density by making the system more isothermal and the anticipated difficulty to pull usable crystals in a low temperature gradient environment.

VI. ACKNOWLEDGMENTS

REFERENCES

1. W. A. Brantley and D. A. Harrison, Proc. IEEE Reliability Physics Symposium, April 1973, p. 267.
2. G. Zaeschmar, AGARD Proceedings No. 219, London, May 1977, paper No. 37, H. Hodara editor, Nat. Tech. Info. Service, Springfield, Va., 1977.
3. R. J. Roedel, A. R. Von Neida, R. Caruso, and L. R. Dawson, J. Electrochem. Soc., *126* (1979), p. 637.
4. E. Billig, Proc. Roy. Soc. *A 235* (1956), p. 37.
5. D. C. Bennett and B. Sawyer, "Single Crystals of Exceptional Perfection and Uniformity by Zone Leveling," B.S.T.J., *35*, No. 3 (May 1956), pp. 637–660.
6. P. Penning, Philips Res. Repts., *13* (1958), p. 79.
7. S. R. Lederhandler, J. Appl. Phys., *30* (1959), p. 1631.
8. R. O. DeNicola and R. N. Tauber, J. Appl. Phys., *42* (1971), p. 4262.
9. S. F. Nygren, J. Crystal Growth, *19* (1973), p. 21.
10. A. Steinemann and U. Zimmerli, in "Crystal Growth," Proceedings of an International Conference on Crystal Growth, Boston, June 20–24, 1966, H. S. Peiser ed., London: Pergamon Press, 1967, p. 81.
11. J. C. Brice and G. D. King, Nature, *209* (1966), p. 1346.
12. J. C. Brice, J. Crystal Growth, *7* (1970), p. 9.
13. T. S. Plaskett, J. M. Woodall, and A. Segmuller, J. Electrochem. Soc., *118* (1971), p. 115.
14. J. C. Brice, J. Crystal Growth, *2* (1968), p. 395.
15. R. A. M. Scott, J. Crystal Growth, *10* (1971), p. 39.
16. H. S. Carslaw and J. C. Jaeger, *Conduction of Heat in Solids*, 2nd ed., Oxford: Oxford U. Press, 1958.
17. S. G. Bankoff, "Heat Conduction or Diffusion with Change of State," in *Advances in Chemical Engineering*, Vol. 5, p. 75, T. B. Drew, J. W. Hoopes, Jr., and T. Vermeulen eds., New York: Academic Press, 1964.
18. E. R. G. Eckert and R. M. Drake, Jr., *Analysis of Heat and Mass Transfer*, New York: McGraw-Hill, 1972.

19. D. Rosenthal, Trans. ASME, *68* (1946), p. 849.
20. M. von Smoluchowski, Annalen der Phys., *48* (1915), p. 1103.
21. See, for example, N. N. Lebedev, *Special Functions and their Applications*, New York: Dover, 1972.
22. S. P. Timoshenko and J. N. Goodier, *Theory of Elasticity*, 3rd ed., New York: McGraw-Hill, 1970.
23. E. Schmid and W. Boas, *Plasticity of Crystals*, London: Chapman and Hall, 1968.
24. D. Laister and G. M. Jenkins, J. Mater. Sci., *8* (1973), p. 1218.
25. H. G. Van Bueren, *Imperfections in Crystals*, 2nd ed. Amsterdam: North-Holland, 1961.
26. A. E. H. Love, *The Mathematical Theory of Elasticity*, 4th ed., New York: Dover, 1944.
27. M. Abramowitz and I. A. Stegun, *Handbook of Mathematical Functions*, Applied Mathematics Series 55, Washington, D.C.: National Bureau of Standards, 1970.
28. A. S. Jordan, J. Crystal Growth, *49*, No. 3 (1980).
29. R. Byron Bird, W. E. Stewart, and E. N. Lightfoot, *Transport Phenomena*, New York: John Wiley, 1960.
30. A. S. Jordan, J. Appl. Phys. (April 1980).
31. P. B. Macedo and T. A. Litovitz, J. Chem. Phys., *42* (1965), p. 245.
32. J. Angilello, R. M. Potemski, and G. R. Woolhouse, J. Appl. Phys., *46* (1975), p. 2315.
33. D. J. Stirland and B. W. Straughan, in *Characterization of Epitaxial Semiconductor Films*, H. Kressel, ed., Amsterdam: Elsevier, 1976, p. 139.
34. W. A. Brantley, J. Appl. Phys., *44* (1973), p. 534.
35. V. Swaminathan and S. M. Copley, J. Am. Ceram. Soc., *58* (1975), p. 482.
36. S. G. Lekhnitskii, *Theory of Elasticity of an Anisotropic Elastic Body*, San Francisco: Holden-Day, 1963.
37. B. A. Boley and J. H. Weiner, *Theory of Thermal Stresses*, New York: John Wiley, 1960.
38. B. N. Grechushnikov and D. Brodovskii, Soviet Physics-Crystallography, *1* (1956), p. 470.
39. E. D. Williamson and L. H. Adams, Phys. Rev., *14* (1919), p. 99.
40. B. A. Boley, J. of Math. and Physics (Studies in Applied Mathematics), *40* (1961), p. 300.
41. Several methods are given in *Moving Boundary Problems in Heat Flow and Diffusion*, J. R. Ockendon and W. R. Hodgkins, eds., Oxford: Oxford U. Press, 1975.
42. W. R. Wilcox, in *Fractional Solidification*, Vol. 1, M. Zief and W. R. Wilcox, eds., New York: Marcel Dekker, 1967, p. 157.
43. B. D. Lichter and P. Sommelet, Trans. TMS-AIME, *245* (1969), p. 99.
44. V. M. Glazov, S. N. Chizhevskaya and N. N. Glagoleva, *Liquid Semiconductors*, New York: Plenum Press, 1969.
45. P. C. Leung and W. P. Allred, J. Crystal Growth, *19* (1973), p. 356.